UNIVERSITY OF CALIFORNIA,
IRVINE

Understanding inorganic and hybrid calcium silicate hydrates at the nanoscale: time-dependent response, thermal properties and simulation techniques

DISSERTATION

submitted in partial satisfaction of the requirements
for the degree of

DOCTOR OF PHILOSOPHY

in Civil and Environmental Engineering

by

Ali Morshedifard

Dissertation Committee:
Assistant Professor Mohammad Javad Abdolhosseini Qomi, Chair
Professor Timothy J Rupert
Associate Professor Mo Li

2021

DEDICATION

To my wonderful family

* * *

KING: Life is simply a journey to nowhere. If you want a change of scenery, you need to get there your own way.
SAITAMA: This is starting to sound hokey!
KING: It seems to me you've got this all wrong. You think being strong means you've reached your destination. I doubt the path to becoming a hero comes to an end with such a cut-and-dried finish line.
SAITAMA: Are you trying to lecture me? It's not like you're some veteran hero.
KING: It's inherently wrong to go into a fight seeking satisfaction from the fight itself. Battling with great courage, working to benefit society, isn't that what it means to be a hero?
SAITAMA: What's with the philosophy?
KING: If that ideal is your goal, you've just begun. There's a long road to walk before you become the strongest hero.
SAITAMA: That's true.
KING: Which means that the pursuit of that ideal still remains. Within you, Saitama, there is a great deal of unrealized potential. If that's true, to say that you've already reached the limit of your growth, well, that starts to sound shallow and arrogant, now, doesn't it?
SAITAMA: That's deep.
KING: What does it actually take to be the ultimate hero? Is it an unwavering sense of justice? The courage to face any hardship? Until you've found the answer to that question, how can you say you feel bored? Those are my thoughts on it, anyway. Plus I read it in a manga!
SAITAMA: Wow. You just blew my mind. The "ultimate hero"! Maybe I should be thinking about what that truly means.

From the anime series "One Punch Man" (S02E09)

TABLE OF CONTENTS

LIST OF FIGURES

LIST OF TABLES

ACKNOWLEDGMENTS

First and foremost, I would like to thank my advisor Dr. Mohammad Javad Abdolhosseini Qomi for granting me the opportunity of a lifetime to pursue my graduate studies in his group at UCI. I not only learned from his vast knowledge in our field, but also his creativity in research and pursuit of original ideas. I am also deeply grateful for his generosity in both his time and resources throughout my PhD, which is any graduate student's dream. A hero is usually a figment of our imagination, I am incredibly lucky to have met my academic hero in real life.

I would like to thank the members of my defense committee, Professors Timothy J Rupert and Mo Li for providing me with valuable feedback and suggestions regarding our research both during my qualifying examination and final defense.

I am also thankful for our collaborators at University of Houston: Dr. Konrad J. Krakowiak and Dr. Amir Moshiri. This work would not exist without their exceptional experimental discoveries regarding hybrid organic inorganic materials. I've learned so much from them and look forward to our future collaborations. I also appreciate the insight and feedback provided by Dr. Matthieu Vandamme regarding our work on time-dependent behavior of C-S-H. I am also forever indebted to my former advisor Dr. Morteza Eskandari-Ghadi who kindled in me a unique passion for science and mathematics.

I would like to thank my "homie", Dr. Amir Saeidi, for his support and friendship during my PhD years. I'm also grateful for many stimulating conversations with friends in our research group: Siavash Zare, Sarah Blaian, Daisuke Sakaniwa, Mehdi Shishehbor, Yong Tao and Jaewoong Hur and many others over the years at UCI.

Last but not least, I would like to thank my parents Monireh and Kazem and two sisters Farnaz and Golnaz who have provided me with unconditional love and support throughout the years.

This work would not be possible without the financial support provided by NSF through Grants No. 1825921 and 1826122 and their contribution is acknowledged.

VITA

Ali Morshedifard

EDUCATION

Doctor of Philosophy in Civil and Environmental Engineering **2021**
University of California, Irvine *Irvine, California*

Master of Science in Civil and Environmental Engineering **2016**
University of Tehran *Tehran, Iran*

Bachelor of Science in Civil and Environmental Engineering **2013**
University of Tehran *Tehran, Iran*

REFEREED JOURNAL PUBLICATIONS

- Ali Morshedifard, MR Garcia, MJA Qomi, A Kosmarlj, "Buckling of thermalized sheets". – Journal of Mechanics and Physics of Solids (2021) DOI: 10.1016/j.jmps.2021.104296.
- Ali Morshedifard, A Moshiri, KJ Krakowiak, MJA Qomi, "Spectral attributes of sub-amorphous thermal conductivity in cross-linked organic–inorganic hybrids" – RSC Nanoscale (2020) 12 (25), 13491-13500.
- DW Gardner, J Li, Ali Morshedifard, S Masoumi, MJA Qomi, PJM Monteiro, R Maboudian, C Carraro, "Silicate Bond Characteristics in Calcium–Silicate–Hydrates Determined by High Pressure Raman Spectroscopy" - The Journal of Physical Chemistry C (2020) 124 (33), 18335-18345.
- A Moshiri, D Stefaniuk, SK Smith, Ali Morshedifard, DF Rodrigues, MJA Qomi, KJ Krakowiak, "Structure and morphology of calcium-silicate-hydrates cross-linked with dipodal organosilanes" - Cement and Concrete Research (2020) 133, 106076
- Ali Morshedifard, S. Masoumi, MJA Qomi, "Nanoscale origins of creep in calcium silicate hydrates" – Nature Communications (2018) 9 (1), 1-10 . (Received Giatech's best paper award)
- Y. Zhou, Ali Morshedifard, J. Lee, MJ Abdolhosseini Qomi, "The contribution of propagons and diffusons in heat transport through calcium-silicate-hydrates", Appl. Phys. Lett. (2017) 110 (4), 043104
- Ali Morshedifard, Eskandari-Ghadi, "Coupled BE-FE Scheme for Three-Dimensional Dynamic Interaction of a Transversely Isotropic Half-Space with a Flexible Structure", Civ. Eng. Infrastructures J. (2017) 50 (1), 95-118

- M. Eskandari-Ghadi, D. Mehdizadeh, Ali Morshedifard, M. Rahimian, "A family of exponentially-gradient elements for numerical computation of singular boundary value problems" - Eng. Anal. Bound. Elem. (2017) 80, 184-198

- M. Eskandari-Ghadi, M. Raoofian-Naeeni, R.Y.S. Pak, A.A. Ardalan, Ali Morshedifard, "Three dimensional transient Green's functions in a thermoelastic transversely isotropic half-space", ZAMM - J. Appl. Math. Mech. (2017) 97, 12, 1611-1624

SOFTWARE

Python, MATLAB, Fortran, Mathematica, bash, Tcl, Regex, C/C++, high-throughput techniques, parallel computing, LaTeX, SMILES/SMARTS, LAMMPS, VASP, Quantum Espresso, VMD, GULP, various Python simulation packages, Abaqus, ANSYS Mechanical APDL/Workbench, Vesta, Avogadro, Linux

ABSTRACT OF THE DISSERTATION

Understanding inorganic and hybrid calcium silicate hydrates at the nanoscale: time-dependent response, thermal properties and simulation techniques

By

Ali Morshedifard

Doctor of Philosophy in Civil and Environmental Engineering

University of California, Irvine, 2021

Assistant Professor Mohammad Javad Abdolhosseini Qomi, Chair

Calcium silicate hydrates (C-S-H), the main product of cement hydration, account for the majority of observed behavior in concrete. Cement production has a devastating environmental footprint and any improvement in its performance through innovative material design can have significant global impact. In this thesis, we first focus on understanding nanoscopic mechanisms underlying time-dependent mechanical response (e.g. creep) in cementitious materials. A viscoelastic behavior is observed at the scale of single C-S-H globules. However, we demonstrate a gradual transition from exponential viscoelastic behavior to logarithmic creep as we morph from intraglobular to interglobular regime. We also propose a phenomenological model for capturing the combined exponential-logarithmic creep of C-S-H. Next, we focus our attention on understanding thermal conduction in hybrid organic-inorganic calcium silicate hydrates. For a prototypical model, we show that incorporating organic chain in interlayer galleries of C-S-H can signficantly reduce thermal conductivity of the material. The vibrational modes are investigated to better understand the origins of this reduction. We find that although contribution of propagating modes is more or less intact, there is a reduction in mode diffusivities which can be attributed to phonon scattering due to organic-inorganic interfaces which ultimately result in the reduced thermal conductivity. As the last part of the thesis, we study a hybrid organic-inorganic C-S-H that our collaborators have been able to

synthesize in the laboratory. Interpretation of X-ray data shows that the precipitated solid has the structure of portlandite with a cross-linked interlayer space. After the structure is resolved, we focus on developing a force field capable of modeling such hybrid systems. Cell parameters and elastic constants computed based on density functional theory (DFT) are used as observables in our fitting process. The computed properties using the developed force field compare well with DFT and experimental results. Finally we demonstrate applicability of the developed force field by calculating thermal conductivity and creep for the hybrid system. The developed force field paves the way for further investigations into properties of novel hybrid materials such as the one considered in this study.

Chapter 1

Introduction

1.1 Significance of research on cementitious materials

Accoring to the Climate Science Special Report (CSSR) created by the U.S government[158], higher temperatures projected for the United States are expected to increase the intensity and frequency of extreme events. This will cause dire global challenges and in particular for the United States such as the following among others:

- *Coastal Flooding.* Global sea level rise has already affected the United States; the incidence of daily tidal flooding is accelerating in more than 25 Atlantic and Gulf Coast cities. Sea level rise is expected to be higher than the global average in some parts of the United States, especially on the East and Gulf coasts of the United States. This is due, in part, to changes in Earth's gravitational field from melting land ice, changes in ocean circulation, and local subsidence.

- *Larger Precipitation Events.* Heavy precipitation, as either rainfall or snowfall, is increasing in intensity and frequency across the United States and the globe. These

trends are expected to continue.

- *Heat Waves.* Heat waves have become more frequent in the United States since the 1960s, whereas extreme cold temperatures and cold waves have become less frequent. Recent record-setting warm years are projected to become common in the near future for the United States as annual average temperatures continue to rise.

- *Forest Fires and droughts.* The incidence of large forest fires in the western contiguous United States and Alaska has increased since the early 1980s and is projected to further increase in those regions as the climate warms, with profound changes to regional ecosystems. As for droughts, Annual trends toward earlier spring snowmelt and reduced snowpack are already affecting water resources in the western United States, with adverse effects for fisheries and electricity generation. These trends are expected to continue.

The rise in such calamities will have a deep detrimental impact on US economy, national security and public safety. To stop or even roll back the adverse effects of climate change, we need to address the root cause which is industrial CO_2 emissions. More than 20 billion tons of concrete produced annually contribute 5–10% to the worldwide anthropogenic carbon dioxide production[155]. This underlines the importance of investment in understanding the underlying mechanisms that results in cement's unique behavior which in turn can help with innovation in designing material that can eventually reduce production and move the industry toward a more sustainable existence by reducing the environmental footprint. Such innovation has the potential for transforming the industry and creating new jobs in the cement industry. Another challenge faced by the United States is its aging infrastructure. According to the American Road and Transportation Builders Association, one in three of America's bridges have identifiable repair needs and the average age of each structurally deficient bridge is 67 years[1]. According to the report, if all bridges would be repaired today, it would cost \$57.8 billion to replace the 34% of our structurally deficient bridges. This means that any

innovation in material design can reduce costs drastically in such projects. Especially of interest for bridges is the issue of creep which in the past has resulted in major damage and even collapse[12]. Aside from structural aspects of concrete, its thermal performance comes to the forefront in certain applications. For instance in recent years, there is a need for drilling pipes in permafrost for oil extraction[24]. If thermal conductivity of concrete is not taken into account, the frozen region around the pipeline could melt which could have devastating consequences such as soil settlement and oil leakage and its devastating environmental impact.

Environmental impact, structural performance and thermal behavior are among many aspects of cement application the could benefit from serious investment and deep scientific research. These are some of the driving force behind the research carried out in this thesis.

1.2 Dissertation goals and outline

The materials studied in this thesis are multiple variants of calcium silicate hydrates (C-S-H) and two types of hybrid organic-inorganic materials: a prototypical layered material based on Tobermorite 11 Åand a Portlandite hybrid. In broad terms, our objective in this thesis is to utilize and in some cases provide simulation tools at our disposal to better understand the underlying nanoscopic mechanisms responsible for various aspects of material behavior. We also utilize experimental findings to guide our decisions regarding modeling hybrid materials.

Chapter 2 explores creep in calcium silicate hydrates. The following are the main overarching questions that drive this part of our research:

- Is it possible to simulate creep using atomistic simulations?
- Does C-S-H have the same creep behavior at nanoscale as observed in larger scales?

- What are the origins of logarithmic creep in cementitious materials?

In this chapter we developed a technique that makes it possible for us to study creep through simulations. Consequently, we discovered a viscoelastic behavior for individual C-S-H particles. We also find that the logarithmic creep observed in most experiments results from a nanogranular behavior among C-S-H particles and is an interglobular phenomenon rather than an intraglobular one.

In the next chapter, we focus our attention on thermal transport in a model organic-inorganic calcium silicate hydrate. The main questions underlying this chapter are:

- How does thermal conductivity in hybrid organic-inorganic calcium silicate hydrates compare with its inorganic counterpart?
- What can we learn by investigating vibrational modes in hybrid systems?
- What are the tools required to carry out a meaningful vibrational analysis in atomistic models?
- What are the origins of the change in thermal conductivity of hybrid materials (if any)

This chapter resulted in a technique for distinguishing propagating modes in complex systems. We also showed that hybrid materials have a reduced thermal conductivity compared to inorganic C-S-H. The underlying mechanisms that cause this reduction were also investigated and we found that a change in character of diffusons is the main contributing reason.

Chapter 4 is dedicated to developing a realistic hybrid organic-inorganic material with cross-linked layers at the nanoscale. We develop a force field which makes it possible to explore various properties of the material. The main questions driving our investigation in this chapter are as follows:

- Can we synthesize a cross-linked hybrid organic-inorganic material in the lab?
- What are the experimental challenges for characterization of such novel material?
- Can we construct a realistic model of such materials for atomistic simulations?
- What are the challenges for developing an accurate force field that can pave the way for exploring material properties beyond what's available through experiments?
- What can we learn through exploring the material using the developed force field?

Chapter 2

Nanoscale origins of creep in calcium silicate hydrates

2.1 Introduction

Like most engineering materials, concrete exhibits a time-dependent response, e.g. creep, when subjected to sustained external or internal load. This type of deformation not only impacts the life expectancy of our aging concrete infrastructure and the associated environmental footprint incurred for its rehabilitation, but also has important resilience implications. While dislocation[62] and shear transformation zones[51] are at the heart of creep in crystalline materials and metallic glasses, the nanoscale mechanisms underlying time-dependent deformation in cementitious materials are complex and still the subject of intensive fundamental research[150]. For calcium-silicate-hydrates (C-S-H), the main binding phase in cementitious materials, this complexity can in parts be attributed to the presence of nanoconfined water, the material's layered structure at the nanoscale[111], its globular texture at the mesoscale[58] and its multiscale porous structure[55]. These complexities further hinder the

inherent difficulty in studying nanoscale longtime phenomena that arise from eighteen orders of magnitude difference between characteristic time scales in atomic vibrations and creep deformation. The majority of the literature focuses on continuum[9], micromechanics[131] and coupled microstructure-continuum models[79] to predict creep in cementitious materials. Currently, a few phenomenological models are available that are calibrated with the goal of predicting a comprehensive database of experimental results[53, 10]. These phenomenological models are critical in predicting long-term deformation of concrete structures, yet their link to fundamental materials physics remains to be understood. Also, the measurement of creep deformation in cementitious materials is further complicated due to coexistence of long-term hydration process[122] and the accompanying shrinkage deformation. The portion of creep deformation that is not due to the hydration process, i.e. non-aging creep, constitutes a significant part of concrete's overall time-dependent deformation and is the subject of this chapter. In an effort to address non-aging creep in C-S-H, microprestress solidification theory proposes the existence of frozen eigenstresses[11] that relax over time following a power/logarithmic relation. Yet, the origins of C-S-H's creep and its link to chemical composition and molecular structure of C-S-H cannot be explained by such phenomenological models and remain vastly unexplored. This calls for a molecular-level investigation of mechanisms behind C-S-H time-dependent phenomena. Molecular dynamics (MD) simulation is the standard approach to explore atomic level processes that occur at the nanoscale. The first challenge in modeling cementitious materials is constructing an initial atomic structure for simulation purposes. Many studies have concluded that a structurally imperfect Tobermorite is a satisfactory model for C-S-H[111, 143, 137] which is the strategy adopted in the current thesis. The next challenge is deriving accurate interatomic interactions such that reasonable agreement with a wide range of experimental observations is obtained from simulations. Several empirical force fields have been applied or developed for modeling C-S-H such as ClayFF[26], CSH-FF[132], CementFF[39] and ReaxFF[32]. For details, the interested reader is referred to a recent comparative review on the subject[99]. Each of these force fields have their strengths and

limitations. Since elastic properties were included when parametrizing CSH-FF, it seems to be more suitable where mechanical properties are the focus of the study and hence it is the force field chosen for the current study. Availability of structures and force fields has spurred research in the cement and concrete community in areas such as free energy calculations[88], heat and mass transport properties[163, 121, 120], polymer/C-S-H composites[133], to just name a few. Despite significant advances, with currently available technology, MD simulations remain constrained to small time scales on the order of microseconds[36]. Since time-dependent phenomena such as creep occur on a time scale of hours, days and even years, a conventional MD simulation proves insufficient. From a probabilistic perspective, a phenomenon such as creep that occurs at long time scales, can be viewed as a rare event process, the procession of a series of rare events[112]. In a non-equilibrium dynamic system such as a viscoelastic material under shear, the majority of the simulation time will be spent in a metastable basin. A jump to a more favorable basin by thermal activation would mean crossing an energy barrier, which requires a fluctuation with a low probability. This turns out to be the underlying cause of the disconnect between the macroscopic and nanoscopic time scales[73]. Biased molecular simulations, e.g. hyperdynamics[152], metadynamics[6] and Autonomous Basin Climbing[73], are among the most noticeable time acceleration techniques. These approaches are limited to problems with small numbers of collective variables and fail for systems with soft modes. This makes their application to C-S-H rather irrelevant due to the presence of many soft degrees of freedom in nanoconfined water molecules. Inspired by experimental procedures in characterizing fatigue[77] and the compaction observed in granular media due to mechanical disturbance[124], to explore time-dependent behavior of C-S-H, we propose a simulation scheme based on the early work of Lacks and Osborne[75]. They applied incrementally increasing shear strain on a binary Lennard-Jones glass and subsequently unloaded the system after reaching a certain strain value. They observed that if the strain limit is small, the system undergoes aging and the internal energy decreases. A single cycle takes the system to a more favorable local minimum in the energy landscape. This approach

artificially accelerates thermal fluctuation induced aging phenomenon. If several of these cycles are successively exerted on the sample, the system progressively visits lower minima same as those visited during a phenomenon such as creep. In this paper, an incremental stress marching technique is utilized to study time-dependent behavior of C-S-H. First, the C-S-H sample is loaded by cyclic perturbations where a relaxation behavior is observed. Subsequently, unloading and re-loading of the sample takes place were a viscoelastic behavior is observed. The simulations show that this simple approach is able to explore different time-dependent regimes of deformation in C-S-H, ranging from creep relaxation to viscoelastic deformation. We finally investigate the impact of water content on the time-dependent behavior of C-S-H and establish its relation to the experimentally observed logarithmic creep.

2.2 Computational model

Atomic structure

C-S-H, the hydration product that is responsible for cement's strength and durability, is a quasi-glassy material with an average C/S around 1.7[70, 125].To make a structure that captures the experimental aspects of C-S-H that exists in ordinary Portland cement such as density, basal spacing and XRD patterns[3, 119, 40], we start from the structure of its natural analogue, Hamid's 11 tobermorite[48], a crystalline mineral with a layered structure composed of infinite dreierketten silicate chains with C/S=1. To avoid finite size effects a $4\times4\times1$ supercell was created with cell parameters $(a, b, c, \alpha, \beta, \gamma) = (13.27, 24.44, 24.44, 89.68°, 90.13°, 123.21°)$. Next, calcium to silicon ratio is increased by removing the bridging sites (charge neutral SiO_2) from the infinite silicate chains of tobermorite. Note that based on NMR experiments, such removal should produce only dimers, pentamers, etc in compliance with the dreierketten rule[116]. Similar atomic models of C-S-H can be constructed by following different procedures

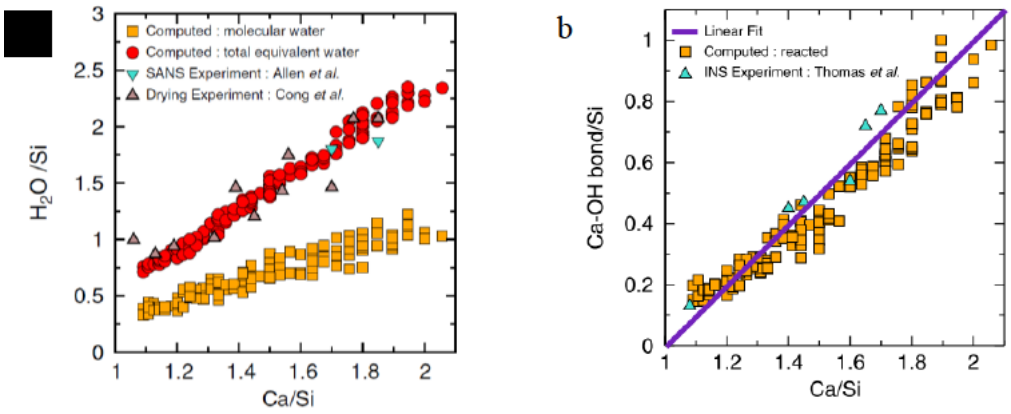

Figure 2.1: Variation of molecular and equivalent water content in C-S-H computed from reactive simulations[119]

as carried out, for instance by Kumar et al. [72] or Kovačević et al. [68]

We note that after full relaxation of the prepared structure using CSH-FF forcefield[132], we have detected a trimer in the final structure. This can be attributed to an artifact of the potential set used and although comparison with other forcefields show that such artifact does not impact the conclusions of this paper, care should be taken when using this structure in more demanding simulations. When all the bridging sites are removed, C/S stands at 1.5. Further increase in C/S is achieved by removing pairing sites from the structure until a C/S=1.7 is reached which is the average value observed in experiments[125]. Next, to charge balance ending oxygen atoms with hydrogen atoms, we use the results of reactive simulations carried out by Abdolhosseini et al as shown in Supplementary Fig. 5.

The model so prepared has 48 Ca-OH bonds, 56 SiOH bonds and 50 water molecules. The final structure contains 634 atoms and the empirical formula is: $Ca_{1.7}Si_{1.0}O_{2.5}(OH)_{1.7}\,(H_2O)_{0.9}$. To model the intraglobular to interglobular (ITI) behavior in the simulations, we gradually increase the water content in the interlayer of the model prepared initially by the previously mentioned procedure. Naturally, the basal spacing needs to be increased to maintain the proper density for water.

Table 7 Average elastic properties of 11 Å tobermorite

	GGA-DFT[11]	ClayFF	Core–shell	CSH-FF
K^{Voigt}/GPa	66.7	40.2	69.6	59.6
G^{Voigt}/GPa	37.8	27.3	36.4	39.6
K^{Reuss}/GPa	55.0	24.8	57.1	47.7
G^{Reuss}/GPa	34.1	20.8	30.1	35.8
K^{VRH}/GPa	60.8	32.5	63.3	53.6
G^{VRH}/GPa	36.0	24.1	33.2	37.7
K^{Vel}/GPa	58.9	35.5	63.2	51.5
G^{Vel}/GPa	34.5	22.0	31.5	36.0

Figure 2.2: Average elastic properties of 11 Tobermorite[132]

Molecular dynamics and force field

Regarding force field, Clay-FF is one of the main set of parameters available for modeling complex hydrated inorganic minerals such as clay and tobermorite[26]. However, it has known deficiencies in reproducing the correct elastic properties for cementitious materials. Table 2.2 adapted from [132] shows a clear comparison between the predictive powers of CSH-FF and ClayFF:

CSH-FF is a ClayFF-based forcefield that incorporates second order properties (i.e. elastic moduli) in the fitting process which makes it the more accurate forcefield when it comes to silicate minerals prevalent in cementitious materials. Consequently, we have utilized CSH-FF in simulations in this chapter. In this forcefield, harmonic linear bonds are defined for the SPC water molecules and hydroxyl groups. Also, we have angular harmonic contributions to energy from water molecules. All the other interactions are captured by non-bonded Lennard Jones and electrostatic potentials. Considering the fact that CSH-FF is also capable of accurately reproducing the cell parameters for cementitious materials, it seems to be the

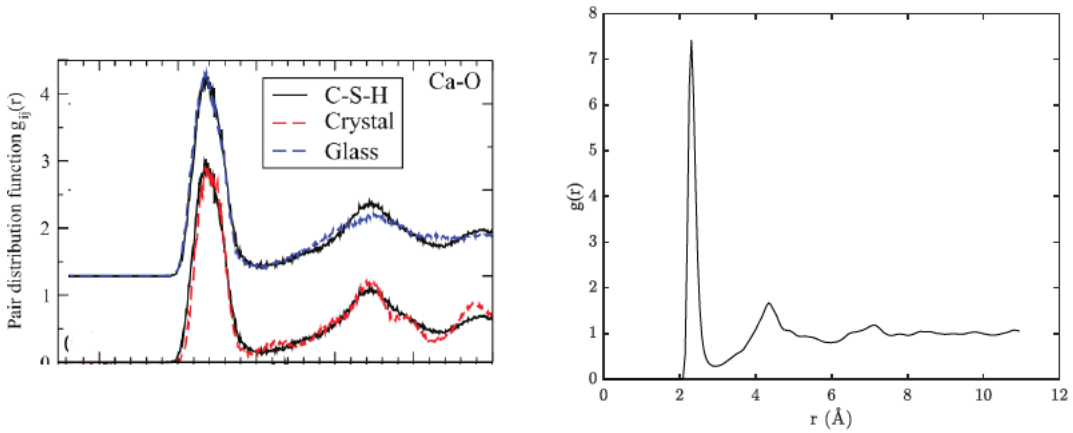

Figure 2.3: Partial pair distribution functions for Ca-O pairs. a) the model used in [119] b) the model used in the current study.

most suitable forcefield available for our purposes. Note that ReaxFF (a bond-order based potential) is an alternative forcefield for cementitious materials that possesses the ability to capture bond breakage/froming during deformation[86]. However, its high computational cost makes it impractical for the current study.

Calcium coordination

To compare the model used in this study and the previous models used in [119], we compare the partial pair distribution function for Ca-O pairs in Supplementary Fig. 6. It is clearly observed that the peaks are narrower in the model used for the current study which indicate a higher degree of order. Moreover, we calculate the coordination of each calcium atom by integrating the PDF up to the first minimum as follows:

$$n(r) = 4\pi\rho \int_0^{r'} g(r) r^2 dr \tag{2.1}$$

where r' is the position of the first minimum. We obtain a value of 5.93 for average coordination number and the minimum coordination of Ca atoms stands at 4.8. Considering the high C/S of the sample, we believe this to be a satisfactory check for the model.

We use LAMMPS simulation package for all computations[115] with Ewald summation for long range electrostatic interactions. All models in our numerical experiments are initially relaxed in the NPT ensemble using Nose-Hoover thermostat[52] at 300 K and Parinello-Rahman thermostat and barostat [109] at 1 atm for 2 ns and time steps of 1 fs. Also, a cutoff of 12 was chosen for non-bonded interactions.

2.3 Artificial aging

shear stress-strain curves for C-S-H

To study time-dependent phenomenon, we create a representative structure of C-S-H as described in the previous section. The stress-strain behavior of our C-S-H models in shear return a value of 21.1 ± 2.1GPa for the shear modulus, which compares well with a value of 21 GPa reported elsewhere[86]. Particular features are noticeable in C-S-H's stress-strain behavior.

First, at strains smaller than 6.5%, the shear stress-strain curve is jagged, while exhibiting a linear behavior on average. This jagged response is indicative of a rugged energy landscape with numerous local minima[84]. Upon unloading from these local minima, a small yet non-negligible residual strain appears that is in the order of 0.1%. This is indeed similar to Lacks and Osborn's observations in binary Lennard Jones systems[75]. Second, C-S-H exhibits a sudden increase in the residual strain in the order of 2%, if loaded beyond 1.5 GPa, which can be viewed as the yield limit.

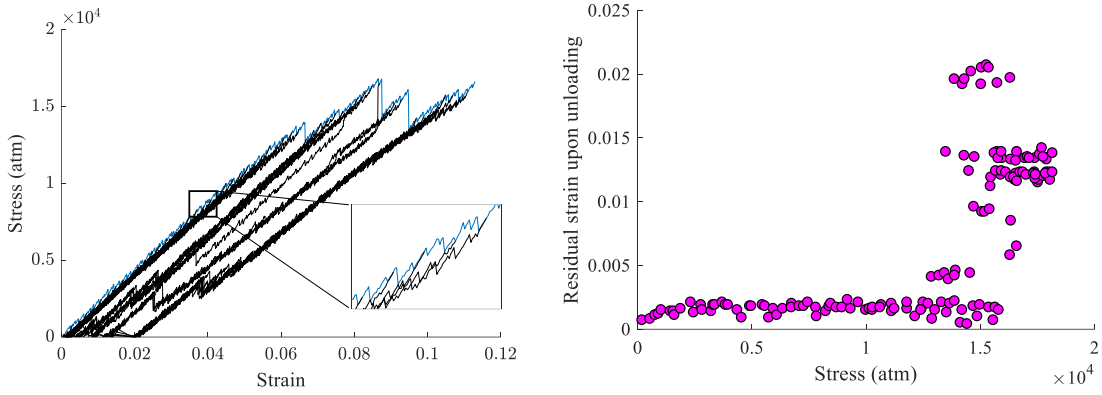

Figure 2.4: Shear loading of the specimen and unloading at different strain values. a) An elastic behavior is observed up to a stress of about 15000 atm. We have unloaded the system at different strain values. It is clearly observed that up to a stress level of about 15000 atm, the system shows negligible residual strain upon unloading. Perturbation values should be chosen in a way that the system remains below the yield stress. b) Residual strain as a function of the stress value where unloading was initiated. The onset of inelastic behavior is observed to be around 15000 atm.

Incremental Stress Marching (ISM) Technique

Here, we envision a three stage cyclic scheme that applies successive stress perturbations with varying average stress levels. To guarantee that ISM explores time-dependent phenomena rather than the failure process, we ensure that the shear stress level at all times remains below the yield limit, $\tau + \Delta\tau < \tau_f$. A complex system such as C-S-H has a rugged energy landscape[75, 56] as discussed in the results section and the core objective of this technique is to facilitate the evolution of the system to the low-lying minima from its current state using gradient-based energy optimization as demonstrated in Figure 2.5a. Our approach continuously monitors the internal energy, enthalpy, stress, strain, and atomic trajectory in molecular models during loading (stage I), unloading (stage II) and reloading (stage III) phases, as demonstrated schematically in Figure 2.5b. In each individual stress cycle, the stress is perturbed about the mean value with increments of 0.01 GPa and an enthalpy minimization is carried out at the end of each increment. This is justified due to the negligible effect of the entropic term in Gibbs free energy for a solid system such as C-S-H ($G = H - TS$

where G, H and S are the Gibbs free energy, enthalpy and entropy of the system). A threshold of ± 0.1 GPa is defined around the mean value and the loading direction is reversed when the limits of the envelope are reached. We use a total of 3×104 stress cycles in our ISM framework, which would ultimately lead to about 2×106 minimization steps. This staggering number of enthalpy minimizations signifies the infeasibility of eigenvalue-based minimizers that ensure convergence to a local minimum. However, unlike stress tapping approach[8], our incremental updated Lagrangian method resolves an artifact of gradient-based minimizers, i.e. the possibility of converging to a saddle point. We note that the ISM technique is computationally expensive due to millions of enthalpy minimizations required in the process.

Cyclic loading and unloading of the models (Stages I and II)

A complex system such as C-S-H has an extremely rugged energy landscape[75, 56] and the core objective of the incremental stress marching technique is to facilitate the evolution of the system to the low-lying minima from its current state using gradient-based energy optimization as shown in Fig. 2.5a.

We subject the molecular structure of C-S-H to cyclic loading with different mean stress levels (stage I in Fig. 2.5b).

As shown in figure 2.7, this causes the structure to experience an incremental increase in shear strain, while the energy of the system drops to an asymptotic value in a matter of roughly 1000 stress cycles.

We observe that the decline in internal energy occurs even when the mean stress level is zero. Similar behavior is observed for axial stress perturbations as seen in figure 2.8.

To understand this behavior, we note that metastability is a characteristic of non-equilibrium systems such as C-S-H at the nanoscale. Using energy optimization, we merely obtain a

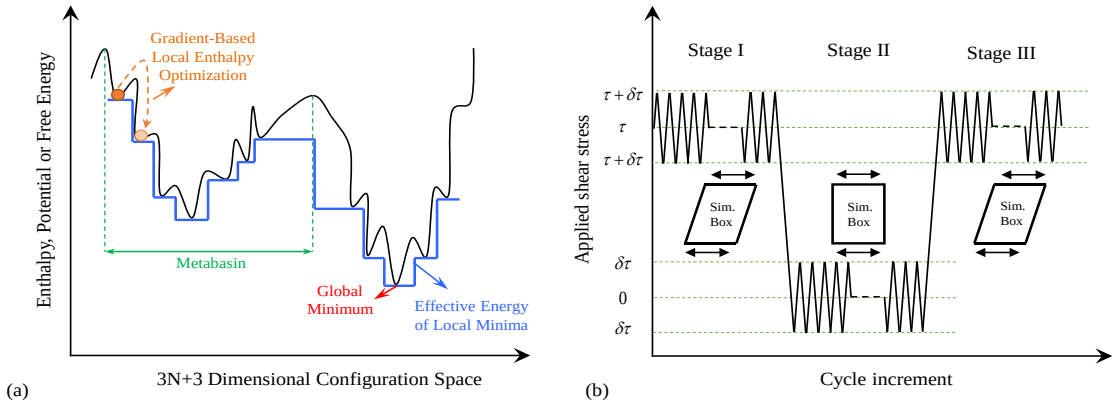

Figure 2.5: Exploring the energy landscape via the incremental stress marching approach. (a) A schematic representation of the energy landscape for a complex system. The orange ball represents the initial state of the system. Applying an external stress and local enthalpy minimization can help overcome the energy barrier, which ultimately takes the system to the minimum of the metabasin. We note that this method would not take the system to an adjacent metabasin that contains the global minimum. (b) Schematic representation of incremental cyclic scheme proposed in this study. The approach contains loading, unloading and reloading sequences, which are demonstrated from left to right. The stress is incrementally perturbed around a mean shear stress level, τ.

structure whose energy is at a "local" minimum. However, due to the metastable nature of C-S-H, the system is still far from the metabasin's minimum in the energy landscape. Reaching this low-lying minimum requires overcoming a series of large energy barriers (hence a very long simulation time). The main objective of ISM is providing a way to reach such favorable minima by a technique other than molecular dynamics. Hence, each cycle of ISM, pushes the system over an energy barrier and into a new local minimum, which is more favorable than the previous one and hence lower in energy. This clearly indicates that we can view stage I as relaxation in shear. We note that the strain values observed here are larger than what is measured in macroscopic experiments[66]. This is due to the fact that the shear is applied parallel to the interlayer spacing and the layers can slide over each other with reduced restriction. However, in mesoscopic length scales such free movements are limited by an interconnected network of C-S-H layers. A realistic mesoscopic model would be needed to investigate such effects. The Kohlrausch-Williams-Watts relaxation function has been extensively used as a phenomenological model to predict relaxation behavior in

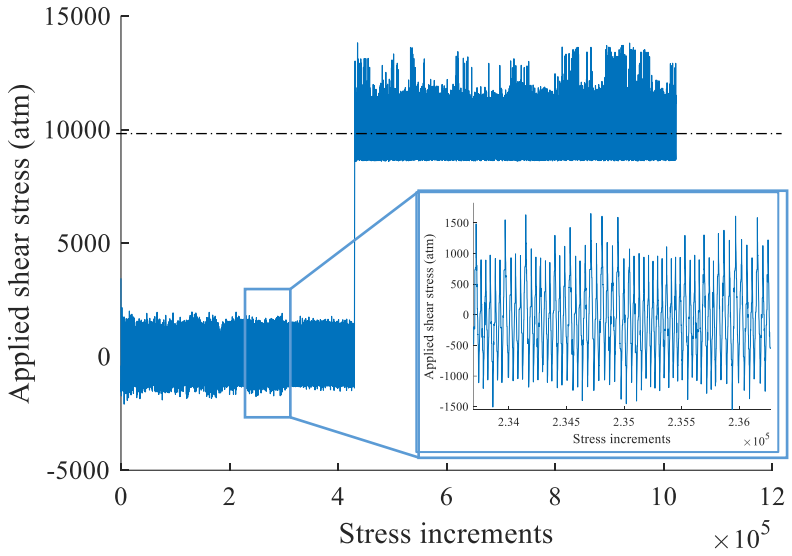

Figure 2.6: Gradual stress perturbations. A seamless transition to the next cycling stage (mean shear stress of 10000 atm) can be observed. As explained in the text, the Incremental Stress Marching technique, consists of load cycles on the specimen with a predetermined average stress. This sample is initially loaded at 0 stress and stress perturbations of $\Delta\tau = 1000$atm are applied. The periodic nature of these stress cycles are demonstrated more clearly by maginification of a portion of the graph.

glass systems[113, 156]. This function can be derived by several models such as hierarchically constrained dynamics[108] or diffusion-trap[113] and exhibits a stretched exponential shear strain as a function of cycles:

$$\gamma = \exp\left(-\left(\frac{N}{N_0}\right)^{\beta}\right) \tag{2.2}$$

where N is the number of cycles overtook, N_0 can be thought of as a characteristic relaxation number, β is the stretching exponent and γ is the engineering shear strain. We find that this function is capable of accurately fitting our data. We also note that the Normalized Root Mean Squared Error (NRMSE) values lie in the interval [0.02, 0.16] for all the fitted curves in this paper. This stretched exponential relation was also proposed when modeling glass relaxation by infliction of axial tapping cyclic stress perturbations[160]. After reaching an asymptotic value of strain and energy in the first stage, we begin stage II by unloading the system and continuing the sequence of stress perturbations. We observe that in the

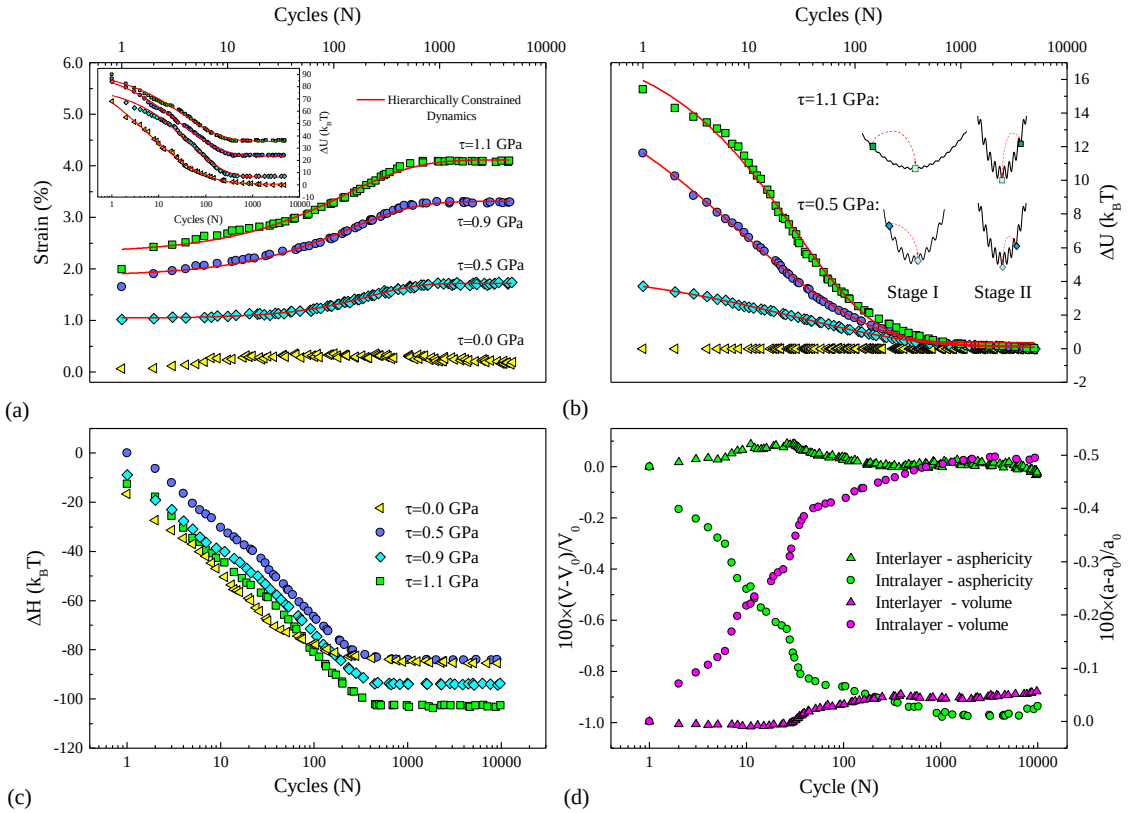

Figure 2.7: Evolution of the system under constant mean shear stress as a function of cyclic perturbations. (a) Strain evolution as cycling progresses for different stress levels. The inset shows the drop in potential energy level during the process. For the case where stress is zero, the strain remains constant, while the energy drops regardless. Such behavior is akin to relaxation phenomena in glasses and can be explained via hierarchically constrained dynamics with stretched exponential behavior. (b) The drop in potential energy during the unloading phase. We observe an exponential relaxation reminiscent of viscoelastic deformation in solids. (c) The decrease in the enthalpy as a function of cycles during the relaxation stage. This indicates that the enthalpy as well as internal energy is minimized in these relaxation processes. (d) The change in average Voronoi volume and asphericity of the atoms in the interlayer and intralayer of the specimens. We observe a significant decrease in characteristics of the Voronoi cell for atoms in the interlayer, while the intralayer attributes remain approximately constant. This highlights the reconfiguration of interlayer constituents as the primary contributor to the relaxation phenomenon at the nanoscale.

course of the second stage, regardless of the stress history (the mean stress applied during the first stage) all systems reach a common value of energy minimum after 5000 cycles (Figure 2.7b). Since we are continuously relaxing box dimensions in our structural optimizations, it is in fact the enthalpy of the system that is minimized. The decreasing trend observed for all cases in Figure 2.7c corroborates this assertion. The distinction between enthalpy and

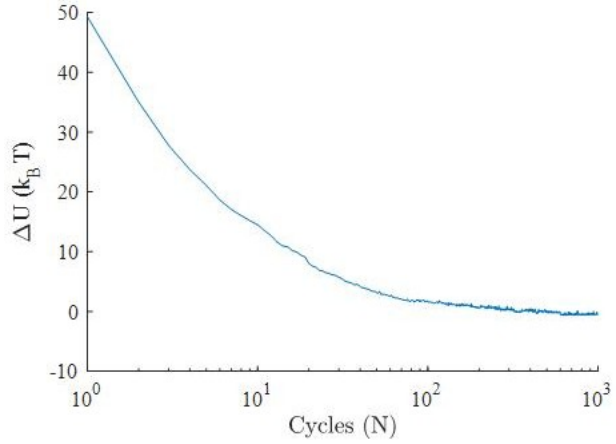

Figure 2.8: Decrease in potential energy as a result of cyclic perturbations on the system in an axial direction. Inflicting cycling stress perturbations to the system in the normal direction, causes a similar decrease in energy as Fig. 2 in the main text. This similarity is expected since cycling at zero stress in any direction signifies relaxation.

potential energy evolution proves more interesting for the third stage as described in the next section. The results in Figure 2.7a-b, can be understood in an enthalpy landscape framework, similar to the approach adopted to explain protein folding in biological systems[81]. A rugged enthalpy landscape can be envisioned for the system as seen by the schematic inset in Figure 2.7b. Initially, the system resides in a metastable state, which is separated from the minimum of the basin by numerous small barriers. Application of external stress, distorts the enthalpy landscape of the system and lowers the secondary barriers in the basin that would ultimately translate to higher transition rates[165]. Malandro and Lacks also showed that application of external shear strain causes the local minima of the potential energy surface to disappear, leading to mechanical instabilities that force the system into unexplored regions of the energy landscape. As seen from the inset of Figure 2.7b, the landscape is transformed again upon unloading and the system is no longer in the minimum of the metabasin. Further cycling will again result in a drop in the internal energy to the lowest lying point in the metabasin, as observed in the inset. To further understand the kinematic sources of relaxation in the C-S-H sample, Voronoi volume and the asphericity of the Voronoi cells were investigated for each atom. Asphericity is defined as the radius of the sphere with the same volume as the

atom's Voronoi cell[135]:

$$\eta = \frac{A^3}{36\pi V^2} \tag{2.3}$$

where A is the total area of the convex hull of the Voronoi cell and V is the Voronoi volume of the cell. At this stage, we distinguish between atoms in the defective intralayer calcium-silicate sheets and those forming the interlayer spacing. We observe a significant decrease in both the average asphericity and Voronoi volume of the interlayer constituents, interlayer calcium, hydroxide and water molecules, while the values for the intralayer atoms remain constant (Figure 2.7d). This can be regarded as evidence that the interlayer species are the main contributors to the time-dependent relaxation of C-S-H globules under constant stress.

Cyclic reloading of the models (Stage III)

If external stress is applied to the system at the end of the unloading stage, an instant increase in energy and shear strain is observed. Moreover, continued cyclic perturbations will cause the energy and strain of the system to further increase as shown in Figures 2.9a-b.

This form of cycle-dependent behavior is akin to that of viscoelastic behavior of solid materials. We verify that the final asymptotic strain scales linearly with the applied stress, see inset of Figure 2.9a. Consequently, we use the phenomenological standard solid model to fit our data. This model, as shown in the inset of Figure 2.9, is composed of two spring elements and a damper. Solving the differential equation governing this model under constant stress, τ_0, leads to:

$$\gamma = \frac{\tau_0}{G_2}\left\{\frac{G_1 + G_2}{G_1} - e^{-\lambda N}\right\} \tag{2.4}$$

where G_1 and G_2 are the instantaneous stiffness and damping stiffness of the elastic compo-

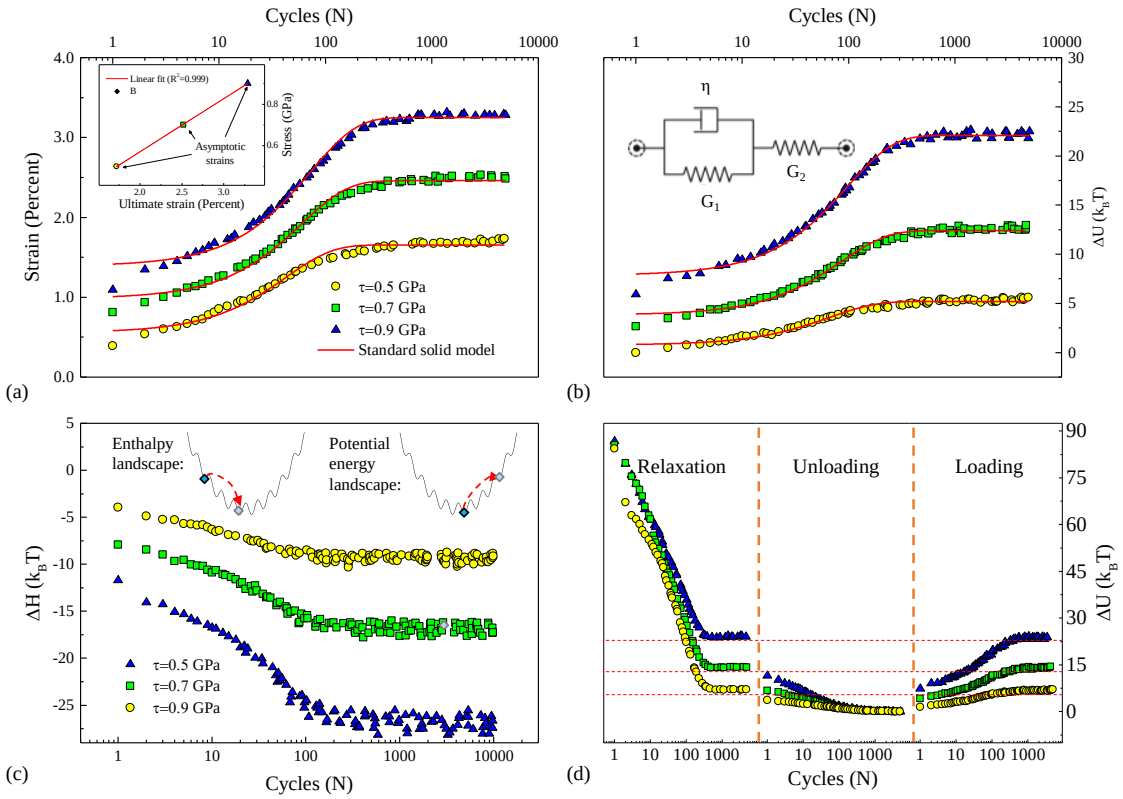

Figure 2.9: Time-dependent characteristics of the reloading stage. (a) Strain as a function of the number of cycles for three different stress levels. The inset shows that the asymptotic value of strain reached at each stress level scales linearly with the applied shear stress. (b) Increase in the internal energy of the system as a function of the number of cycles. The inset shows the standard solid model used to fit the atomistic simulation data. (c) The decrease in enthalpy as a function of the number of cycles, regardless of the applied stress level. The inset schematically represents the evolution of the system in both the enthalpy and potential energy landscapes. While the potential energy of the system increases by climbing the energy landscaoe, the enthalpy decreases gradually to achieve thermodynamic equilibrium state. (d) A holistic view of the loading, unloading and reloading sequences that signifies the irreversibility of the relaxation process and reversibility of the viscoelastic behavior.

nents, $\lambda = \frac{G^2}{\mu_0}$, and μ_0 is proportional to the viscosity of the material. We obtain a value of $G = 28.8 \pm 1.3$GPa for the average of the resultant shear modulus. Although this has the same order of magnitude as those calculated in direct shear (21.1 ± 2.1GPa), the discrepancy is non-negligible. This can in part be attributed to the approximate linear relationship that is assumed between time and number of cycles. To further understand the observed viscoelastic phenomenon, rugged enthalpy and energy landscapes can be imagined for this complex system (inset of Figure 2.9c). As the specimen is loaded, the system is seen climbing

from the minimum of the basin to higher levels of potential energy. If we load a standard solid, we will observe the same behavior. This might seem counter-intuitive, however a glance at the evolution of the system enthalpy (Figure 2.9c) shows a decrease as stress perturbations continue. This means that with each cycle the system is moving to a more favorable minimum in the enthalpy landscape. Viscoelasticity also asserts that the system should recover the initial configuration and energy without any residual deformation. This is proven to be the case for C-S-H, as we note that in Figure 2.9d the final energy state in stage I coincides with the final energy state in stage III.

Intraglobular to interglobar transition

The exponential viscoelastic behavior observed so far differs from the logarithmic creep observed in nanoindentation experiments carried out by Vandamme and Ulm[149], where nanogranular behavior of C-S-H is cited as the origin of creep. According to nano-granular theory, C-S-H mesotxture can be viewed as the assembly of colloidal C-S-H nanoparticles of imperfect tobermorite-like minerals[58]. This theory was hypothesized on the basis of observations obtained from small angle X-ray and Neutron scattering as well as statistical nanoindentation experiments[148, 3, 140]. A simultaneous look at the experimental results and those obtained by atomistic simulations for models with different water content, raises the question: is creep caused by sliding of calcium silicate layers over each other as envisioned by the Feldman-Sereda model[35] or by the nanoglobular mesoscopic behavior. To address this question, we try to reproduce the sliding of C-S-H layers by investigating samples with different water content in the interlayer. In fact, inter and intra-globular behavior of C-S-H can be potentially explored by merely adjusting the number of interlayer water molecules as shown by the atomistic simulation boxes in Figure 2.10a.

Note that in the current study, intraglobular water and interlayer water denote the same

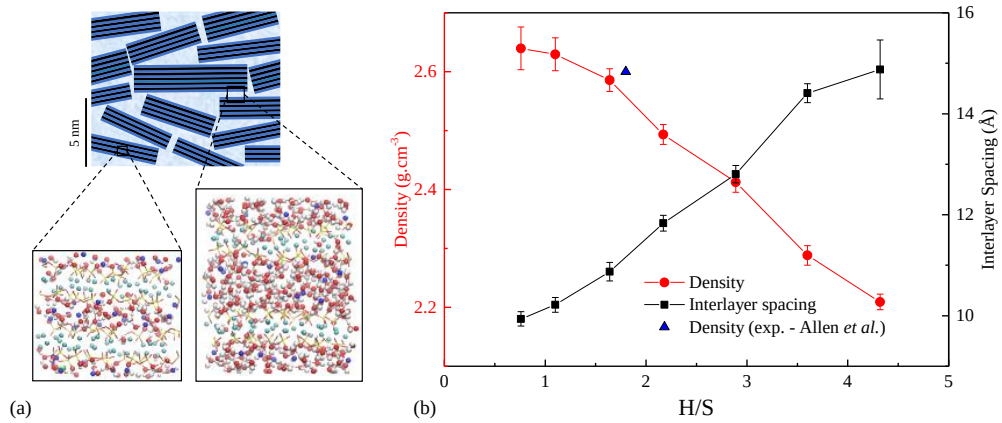

Figure 2.10: The impact of the nanoconfined water content on the morphology, structure and density of C-S-H. (a) Schematics of C-S-H globules at the mesoscale shows how atomistic models with varying interlayer water content can potentially correspond to the inter and intraglobular behavior of C-S-H. The black strips represent silicate layers, dark blue is the intralayer or adsorbed water and light blue is the water between nano-globules of the C-S-H. In the atomistic models, red represents oxygen, blue is interlayer calcium, cyan shows intralayer calcium and white and yellow represent respectively hydrogen and silicon atoms. (b) Variations of density and interlayer spacing as a function of H/S and comparison with Small Angle Neutron Scattering density measurements.

constituents and can be used interchangeably. Here, we choose seven samples with varying water-to-silicon molar ratio (H/S), Figure 2.10b. These samples are prepared simply by introducing more water molecules in the interlayers of the C-S-H model used for previous sections. We find that while the interlayer spacing increased linearly with water content, the density decreases linearly with it. We also investigate the behavior of amorphous ice, the structure of which can be obtained by quenching a thermal simulation box of water using structural optimization (infinitely fast). The amorphous ice sample can be regarded as the limiting case for the C-S-H water content (H/S $\rightarrow \infty$). We first fully relax these eight models by subjecting them to 104 stress cycles and subsequently reload them to monitor their behavior during stage III (Figure 2.11a).

For samples with low water content, a purely exponential viscoelastic behavior is observed. However, as the water content increases, a logarithmic non-asymptotic component emerges. These results show a transition from a purely exponential viscoelastic behavior to a mixed

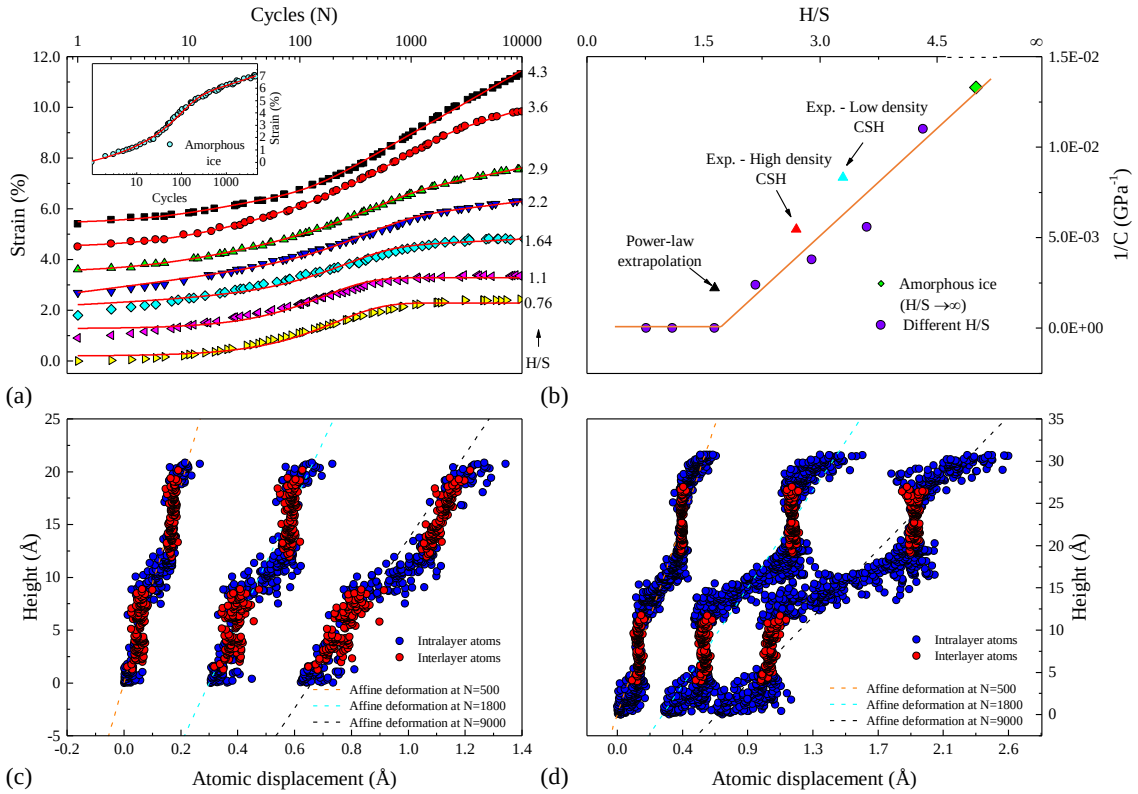

Figure 2.11: The impact of nanoconfined water content on the time-dependent properties of C-S-H during reloading stage. (a) A logarithmic component gradually appears as the water content increases. The inset shows the same experiment carried out on a box of amorphous ice. The graphs have been shifted for clarity. (b) Variation of creep compliance with the nanoconfined water content and their direct comparison with experimental values for the high and low density C-S-H using nanoindentation technique. A transition is observed in the region, where intraglobular water appears. We can also see how the values converge to the case of a box of amorphous ice in the limit. (c, d) Horizontal deformation of the sample with height for a sample with low water content in (c) and high water content in (d). While at high H/S ratio the layers freely slide over each other without distorting the solid constituents, the sliding forces at lower H/S content interlocks adjacent layers that promotes the shear deformation of the solid parts. This implies that the design of non-aging C-S-H materials is closely tied to molecular manipulation of interglobular interlocking structural motifs.

exponential-logarithmic one. To capture this behavior quantitatively, we propose the following phenomenological function for samples with higher water content:

$$\gamma(N) = \frac{\tau_0}{G}\left(1 - \exp\left(-\frac{N}{N_0}\right)\right) + \frac{\tau_0}{C}\log\left(1 + \frac{N}{N_0'}\right) \tag{2.5}$$

where $1/\mathrm{C}$ and N_0 are respectively creep compliance and characteristic number of stress

perturbations. The exponential part of this equation is inspired by Equation 2.5 and the logarithmic part can be interpreted according to experimental observations in nanoindentation tests52. The direct measurement of H/S at the mesoscale proves difficult. Here, we estimate H/S for experimental data based on the reported packing fraction, η, as follows:

$$\left(\frac{H}{S}\right)_{\text{total}} = \left(\frac{H}{S}\right)_{\text{CSH}} + \frac{(1-\eta)\rho_{\text{w}} m_{\text{sim}}}{M_{\text{w}} n_{\text{si-sim}} \eta \rho_{\text{CSH}}} \tag{2.6}$$

where ρ_w and ρ_{CSH} are respectively the density of water and C-S-H. m_{sim} is the mass of the simulation box in g.mol^{-1}, $n_{\text{si-sim}}$ is the number of silicon atoms in the simulation box, and M_w denotes the molecular weight of water in g.mol^{-1}. We find that creep compliance measured for low and high density C-S-H in nanoindentation experiments is close to calculations from our atomistic simulations, Figure 2.11b. The transition of behavior from purely exponential to a combined logarithmic-exponential brings us to the conclusion that each individual globule behaves viscoelastically. However, their sliding over each other, which is modeled by a larger separation of layers with interglobular water, introduces a logarithmic behavior. In other words, these results confirm the hypothesis that creep of hydrated cement originates from reconfiguration of C-S-H globules at the mesoscale rather than sliding of individual C-S-H sheets over each other. To get a better understanding of the underlying cause of the transition of behavior from exponential to logarithmic, deformation profiles are plotted in Figures 2.11c-d for specimens with different water content at several stages during the cycling process. It can be clearly observed that for the case with higher water content (H/S>1.7), the layers can easily slide over each other and there is a negligible shear deformation in the solid part of the C-S-H layer and the deformation only arises from the interlayer constituents. This is partly facilitated by weaker hydrogen bonds in the interlayer compared to the stronger iono-covalent bonds in the silicate backbone56. However, for the case with lower water content (H/S<1.7), a frictional interlocking exists between the motifs of the layers and larger energy barriers should be overcome for sliding to happen. This observation is in agreement with

a decreasing trend observed previously for elastic constants as a function of H/S[31]. The energy barriers and their dependence on the interlayer spacing have been recently studied by Masoumi et al.[88].

2.3.1 Model Dependency

(warning: the note from supplementary materials should be incorporated into this) First, we note that the results presented in this paper, have been obtained based on a model prepared via a similar procedure as explained in Abdolhosseini Qomi et al.[119]. However, there are other more ordered models available in the literature such as those proposed by Kumar et al.[72] and Kovačević et al.[68]. We have applied ISM to these models and also a completely crystalline sample of tombermorite and a similar behavior as the model used herein was observed (Supplementary Figs. 13-17 and Supplementary Note 5). This points to the fact that the layered structure and interlayer spacing can be taken as the main contributors to the time-dependent behavior of C-S-H and other minor structural modifications do not change the overall behavior.

2.4 Discussion

In this chapter, stress induced time-dependent behavior of C-S-H was investigated by application of a chain of aging shear cycles at the nanoscale. We showed that if a C-S-H atomistic model is subjected to repeated aging/rejuvenation cycles under a constant shear stress, the potential energy of the system will decrease until an asymptotic value is reached. This is akin to relaxation in glassy systems and can be explained using stretched exponential hierarchically constrained dynamics model. Voronoi and asphericity analysis of the model during relaxation show that shear relaxation of C-S-H is rooted in reconfiguration of interlayer constituents. In

addition, re-loading the specimen after the relaxation stage will result in an increase in the potential energy of the system. We show that in spite of this increase, enthalpy still decreases, which means the system is moving to more favorable minima in the enthalpy landscape. We also demonstrate that this stage can be well described by a three-component standard solid model, akin to an exponential viscoelastic behavior. We observe a transition window, where the behavior changes from purely exponential to combined logarithmic-exponential behavior with increasing interlayer water content. A combined logarithmic-exponential function was also proposed for a phenomenological description of the observations. An in-depth analysis of shear deformation at the atomic level demonstrated the effectiveness of the shear locking mechanism as a potential venue to restrain non-asymptotic time-dependent behavior. Despite the abovementioned striking observations using a rather simple approach, this work can benefit in many ways from future research at the intersection of cement and concrete science, molecular simulation and statistical physics. Considering the complexity in modeling cementitious materials, we note that using a non-reactive classical force field limits our simulations to non-aging creep. Investigation of aging creep, i.e. creep associated with chemical reactions[2] (breakage and formation of covalent bonds and deformation induced dissolution-precipitation mechanisms), can be conducted using a reactive potential in conjunction with the incremental stress marching technique (ISM). This could be computationally prohibitive, due to the large number of enthalpy optimizations and the associated cost of employing reactive potentials. This motivates further research toward devising algorithms to reduce the cost of reaching a low-lying minimum. Furthermore, to truly test the observed intraglobular to interglobular transition behavior, prohibitively large atomistic models would be needed. This calls for realistic upscaling of C-S-H atomistic models through proper coarse-graining techniques and applying ISM to the model at the larger length scale. Regarding composition of C-S-H, one expects fewer bridging silicate tetrahedra to be present at higher calcium to silicon ratios (C/S). This means that the barriers due to steric repulsion will be altered significantly and time-dependent behavior could possibly be affected. Moreover, previous

research has shown that the number of hydrogen bonds increases with C/S which alters the interlayer hydrogen bond network[120]. A separate study should be carried out to unravel the role played by composition. From statistical physics standpoint, presence of small energy barriers[98] in a complex system such as C-S-H limits the applicability of existing accelerated dynamics techniques. A future progress in this field can potentially unlock the true dynamic trajectory of long-term time-dependent response of structural materials. Assuming that the transition state theory is applicable for studying C-S-H time-dependent behavior[33], the height of barriers separating two inherent structures, i.e. local minima, governs transition rates. Measuring the energy barriers for C-S-H, using methods such as Nudged Elastic Band[59], proves futile due to the presence of many soft modes in nanoconfined water. This means that establishing a link between time and number of cycles in ISM would only be qualitative at best. (warning: Supplementary Note 2 and Supplementary Figs. 7-10 discuss a derivation using a simplified 1D synthetic energy landscape (SEL). However, similar results can be obtained more rigorously using higher dimensional SELs such as NK or transition matrix models62.) Altogether, the results of this work shed more light on various aspects of fundamental mechanisms that cause time-dependent behavior in C-S-H. Furthermore, acceleration techniques such as the proposed ISM would bridge the existing gap between time scales in atomistic simulations and nanomechanical testing of condensed phases, which would ultimately pave the way for rational design of construction materials, and other glassy systems such as oxide and metallic glasses with reduced aging characteristics.

Chapter 3

Thermal transport in hybrid organic-inorganic layered materials

3.1 Introduction

Organic-inorganic hybrids have found impressively diverse applications in a broad range of industries from electronics to separation technologies.[129] They are used in fuel/solar cells[74], photoelectrochemical water splitting[37], water treatment and separation processes[157], Li-batteries[136], and thermoelectric energy conversion[96] to name just a few (see Mir et al. for a recent review[97]). Recently a broad categorization of such materials has been proposed where organics-in-inorganics hybrids (inorganic materials modified by organic moieties) are distinguished from inorganics-in-organics materials (organic materials or matrices modified by inorganic constituents)[139]. Such hybrid materials can also be tailored for thermal applications for instance in building thermal insulation[57, 69], oil wells[54] or pipelines[161, 5] in permafrost regions, and thermal barrier coatings[25]. What makes such materials particularly attractive for thermal management is that we can achieve thermal

conductivities lower than the amorphous limit[20, 18, 101] set by their constituents (e.g., silicates and polymers)[76, 29].

Such exotic reduction in thermal conductivities is intimately related to the presence of nanoscale interfaces between dissimilar constituents regardless of whether they have a layered nanostructure or not. For instance, a significant reduction in thermal conductivity of amorphous silicon/germanium superlattices can be achieved due to the Kapitza resistance at the interface between the two constituent layers [41]. Similarly, Au-Si superlattices can also be tailored to achieve ultralow thermal conductivity[30]. Such effects have also been observed when dispersing silicon nanoparticles in polystyrene matrix [60, 146].

An important category of hybrid materials that remains less explored (regarding both atomic structure and thermal conductivity) is cross-linked layered organic-inorganic hybrids. Cross-linking inorganic surfaces at the nanoscale remains experimentally challenging[91, 95]. Currently, it is achieved by methods such as atomic/molecular layer deposition[118] or electrohydrodynamics[145]. Only recently, covalent cross-linking of calcium-silicate-hydrate layers was achieved using dipodal organosilanes via a sol-gel chemistry technique [106]. Few studies in the literature address thermal conductivity of such materials. Liu et al.[80] measured cross-plane thermal conductivity and volumetric heat capacity for zincone thin films prepared by atomic/molecular layer deposition techniques. Similar results were found by Giri et al. for TiO_2 and ZnO based superlattices with periodic inclusion of organic hydroquinone layers[42]. Losego et al.[82] were also able to utilize a simple self-assembly approach to synthesize organoclay nanocomposites and measure their thermal conductivities using time-domain thermoreflectance. On the atomistic simulation front, recently, Qian et al.[117] developed a force field for organic-inorganic hybrid systems ($\beta - \mathrm{ZnTe(en)_{0.5}}$) and calculated their thermal conductivity using equilibrium molecular dynamics. A common result among such studies is the low/ultra-low thermal conductivities observed in hybrid materials compared to their constituents. Furthermore, the reason for this reduction is

commonly attributed to the fact that interfaces impede phonon transport, but a quantitative physics-based clarification of the origins of this reduction seems to be missing. This motivates an in-depth investigation of modal heat transport and characterization of modal vibrations in cross-linked organic-inorganic hybrid materials.

Our objectives in this chapter can be stated broadly as: 1- Construction of a model cross-linked organic-inorganic hybrid material and understanding its structural features through free energy calculations. 2- Investigating the impact of organic inclusion on thermal conductivities. 3- Explaining the observed conductivity values through a comprehensive modal analysis. We have chosen 11 Åtobermorite (TB) as our base inorganic material. Dipodal organosilanes with different lengths are grafted to opposing surfaces of TB layers to construct cross-linked organic-inorganic hybrids (XTB). This model only serves as a prototype for this class of layered organic-inorganic hybrids. Using molecular dynamics simulations, we first investigate variations in the basal spacing of hybrid samples with different grafting density and polymer length. Guided by potential-of-mean-force (PMF) calculations, we show that the drift of inorganic layers is the main reason behind the reduction in the basal spacing in hybrid samples at low grafting densities. Next, we use the fluctuation-dissipation theorem-based Green-Kubo approach to calculate the thermal conductivities from equilibrium simulations and show a reduction of up to 40% in heat conductivities in hybrid materials. To further understand the origins of this reduction, a full modal analysis is performed. We use a comprehensive and complementary set of computational techniques to characterize and categorize all vibration modes. We demonstrate that reduced mode diffusivities are the main cause of diminished thermal conductivities in our hybrid system (i.e. cross-linked tobermorite or XTB).

3.2 Methods

Computational model

To construct the cross-linked models, we start from the structure of 11 Å tobermorite derived by Hamid [48]. Organosilanes with formulas $(CH_2)_n(SiO_3)_2$ with $n = 2, 4, \ldots, 12$ are grafted to tobermorite surfaces by substituting two bridging sites with each silicate tetrahedra in the organic molecule. Currently, several force fields are available for modeling inorganic C-S-H (e.g. CSHFF[132, 103], CementFF, etc.[100]). Moreover, there are force fields that focus on modeling organic/bio compounds (e.g. CVFF[27] and PCFF[16]). However, due to the presence of organic-inorganic interfaces in our systems, we have chosen the INTERFACE force field[49]. The parameters used in this study are an extension of CVFF for tobermorite minerals. After the model setup, we run molecular dynamics simulations in the NPT ensemble in LAMMPS[114] to equilibrate the system. Nosé-Hoover thermostat and barostat[127] with a time step of 1fs were used for sampling in the NPT ensemble. The basal spacing can be obtained from the ensemble average of the z component of the cell vector.

Potential of mean force

For free energy calculations, we put the same number of organosilanes present in the composite samples on a regular grid. The distance between the center of mass of silica tetrahedra is taken as the collective variable (CV), λ. The potential-of-mean-force (PMF) for this CV is calculated by integrating the mean force, as follows[107]:

$$A(\lambda) = -\int_{\lambda_{min}}^{\lambda} \langle F(x) \rangle \mathrm{d}x \tag{3.1}$$

Modal analysis and thermal conductivity

The thermal conductivity tensor is computed using the so-called Green-Kubo formalism:

$$\mathbf{K} = \frac{V}{k_B T^2} \int_0^\infty \langle \mathbf{J}(0) \otimes \mathbf{J}(t) \rangle \, \mathrm{d}t \tag{3.2}$$

where $\mathbf{J}$ is the heat flux vector, k_B is the Boltzmann factor, T is temperature and V is the simulation cell volume. See Qomi et al.[121] for more details. Vibrational density of states (VDoS), $g(\omega)$, is computed from the Fourier transform of velocity auto-correlation function as[154]:

$$g(\omega) = \frac{1}{N k_B T} \sum_{j=1}^{N} m_j \int_{-\infty}^{\infty} \langle \mathbf{v}_j(t) \cdot \mathbf{v}_j(0) \rangle e^{i\omega t} \mathrm{d}t \tag{3.3}$$

where N is the number of atoms, m_j and $\mathbf{v}_j$ are mass and velocity vector of atom j, respectively.

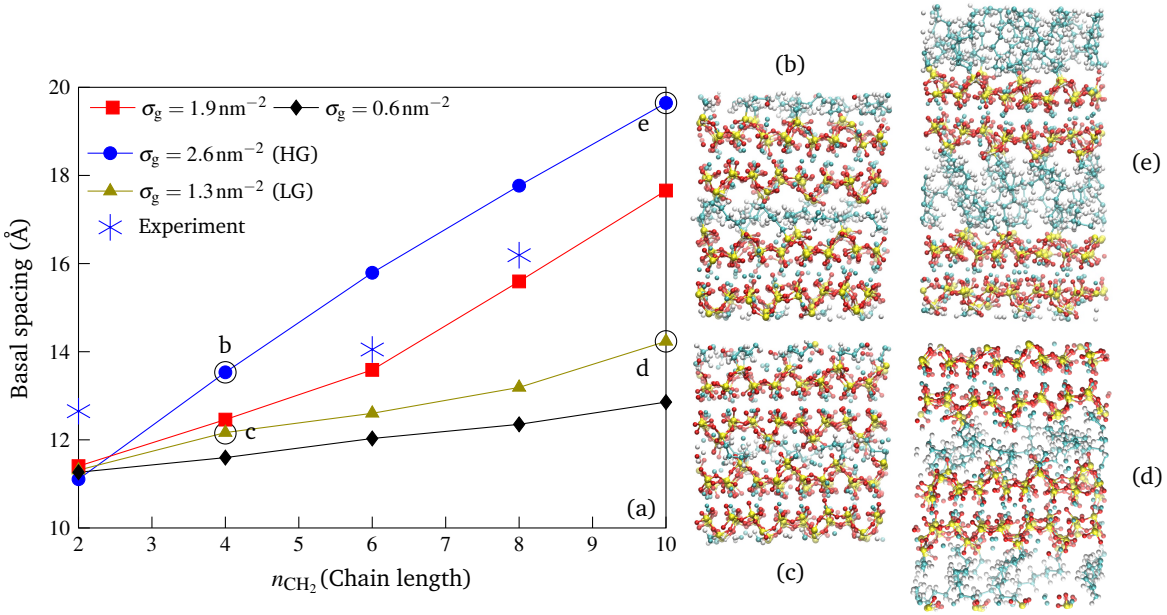

Figure 3.1: Structural results after relaxation (a) Variation of basal spacing as a function of grafting percentage and polymer length (Experimental results after Moshiri et al.[106]). (b-e) relaxed structures corresponding to the circled points on the plot.

To study the mode localization, i.e. the spatial extent at which atoms are involved in a given vibrational mode, we calculate the participation ratio[14] for each eigenvector j:

$$P^j = \frac{1}{N \sum_{i=1}^{N} |\boldsymbol{\varepsilon}_i^j|^4} \tag{3.4}$$

where $\boldsymbol{\varepsilon}_i^j$ is the polarization vector of atom i in mode j, while $\sum_{i=1}^{N} |\boldsymbol{\varepsilon}_i^j|^2 = 1$. While the participation ratio of 1 means all atoms participate in a given mode, a P value close to zero means the mode is localized to a small group of atoms [164]. A threshold can be set such that modes with a small P value can be designated as a localized mode.

Characterizing phonon-like propagating modes in amorphous materials is more challenging than detecting localized modes. Usually, the structure factor is employed for this purpose[34]. However, it is not clear how this can be applied in an anisotropic and inhomogeneous setting such as hybrid materials. Recently, an ad-hoc formula has been proposed for computing a quantity called “eigenvector periodicity", which reportedly helps with distinguishing propagons[130]. Here, we propose a method based on a direct discrete Fourier transform of normalized eigenvectors. This is similar, in spirit, to the work of Kaya et al.[63] carried out on disordered colloidal solids. For each vector in the k-space grid (generated compatible with the periodicity of the simulation box and interatomic distances), we then have:

$$\gamma^k(\mathbf{k}_r) = |\sum_{j=1}^{N} \sum_{\alpha=1}^{3} \varepsilon_{j\alpha}^k(\mathbf{r}_j) e^{-i\mathbf{k}_r \cdot \mathbf{r}_j}| \tag{3.5}$$

where $\varepsilon_{j\alpha}^k$ is the α component of polarization vector of atom j and $\mathbf{k}_r$ is rth wavevector in k-space and $\gamma^k(\mathbf{k}_r)$ is the amplitude of sum of Fourier transforms of each component of eigenvector k for wavevector $\mathbf{k}_r$. If a mode has an underlying frequency resembling a $\mathbf{k}_r$ wavevector, $\gamma^k(\mathbf{k}_r)$ will have a large value. In other words, such modes will have at least one outlier within the data set $\{\gamma^k(\mathbf{k}_r) \mid r = 1, 2, \ldots, n\}$. To detect if a data set contains such an outlier or not, we use the absolute value of standard score (known as the z-score) commonly

used in statistics:

$$z_r^k = \left| \frac{\gamma^k(\mathbf{k}_r) - \mu^k}{\sigma^k} \right| \tag{3.6}$$

where μ^k and σ^k are the mean and standard deviation of the dataset for mode k. Similar to participation ratio, a threshold can be used to determine if a mode has outliers among amplitudes calculated for various wavevectors and if it does, it can be categorized as a propagon, i.e. phonon-like propagating mode.

Limits of propagon,diffuson and locon regions of the spectrum should be prescribed. Given that locons are determined based on participation ratio (a well-established technique), certain values have been proposed in the literature for the locon-diffuson limit[130]. However, as regards the propagon-diffuson limit, since we are proposing a new technique, a decision has to be made regarding the threshold. Since the final formulation is cast in terms of statistical z-scores, an appropriate value can be adopted considering a probabilistic interpretation. We note that ultimately the categorization is to some extent subjective which is analogous to how the electromagnetic spectrum is divided into segments, namely ultraviolet, X-rays etc.

The last method used in this chapter is the formula proposed by Allen and Feldman (AF) for computing mode diffusivities[4]:

$$D_i = \frac{\pi V^2}{3\hbar^2 \omega_i^2} \sum_j^{\neq i} |S_{ij}|^2 \, \delta(\omega_i - \omega_j) \tag{3.7}$$

where S is the heat current operator and V is the cell volume and ω_i is the frequency of mode i. From these, we can compute the diffusive thermal conductivity as $\kappa_{\text{diff}} = \frac{1}{V} \sum_i C_i(T) D_i$, where C_i is the heat capacity of mode i. GULP[38] software is used for calculating mode diffusivities in our systems.

3.3 Results and discussion

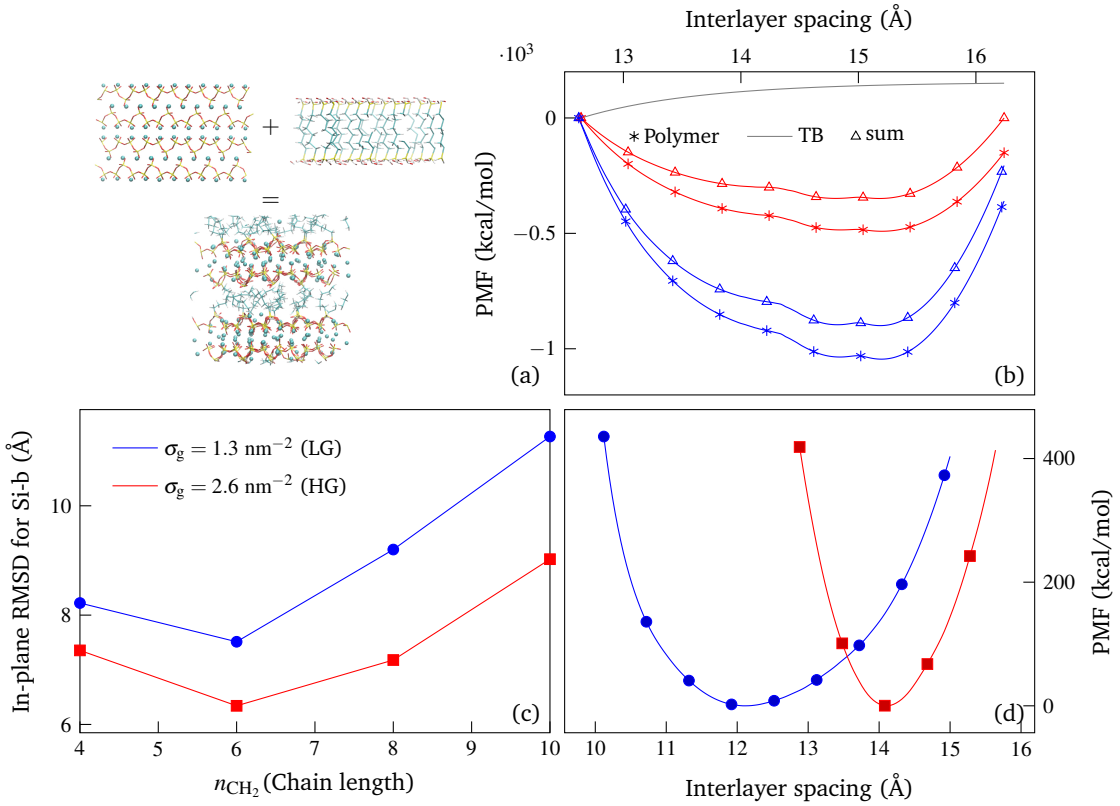

Figure 3.2: Leveraging PMF calculations to understand the underlying reasons for observed basal spacing values (a) Potential of mean force (PMF) for $n_{CH_2} = 4$ for high and low grafting (HG and LG respectively) from polymer chains is summed with that of tobermorite (TB). The shift in position of mimima is negligible. The schematic in (b) demonstrate the concept. (c) RMSD for in-plane displacement of grafted bridging silica (Si-b). There is a significantly larger drift for the layers in samples with lower grafting. (d) PMF for real configuration of polymers extracted from relaxed composite structures

The first structural information obtained from our simulations is the basal spacing, as shown in Figure 3.1. σ_g denotes the number of grafted polymers per surface area and n_{CH_2} denotes the number of CH_2 units in the organosilane polymer (chain length). As expected, the basal spacing increases almost linearly as a function of polymer size[106]. Our recent experimental findings[106] on hybrid systems with a similar structure are compatible with these results as shown in Figure 3.1. In these experiments, we were able to synthesize hybrid calcium silicate hydrate gels of controlled stoichiometry, and via a sol-gel process using dipodal organosilanes

(bis-alkoxysilanes) of alkyl chain lengths (n_{CH_2}) ranging from 2 to 8. The nanostructures were characterized with various techniques including X-ray diffraction (XRD). Presented experimental results, Figure 3.1, are derived from high-resolution XRD experiments carried out in the low 2θ ($3^\circ \sim 15^\circ$) range, which encompasses the basal reflection of the hybrid systems. More details on synthesis protocols, characterization results and molecular structure can be found in Moshiri et al[106].

In experiments carried out on clay composites, Losego et al. were also able to control the interlayer spacing by varying chain length and trends similar to those observed in our simulations were obtained[82]. However, experiments are silent on grafting surface densities, σ_g. Figure 3.1 shows an interesting phenomenon: we have smaller basal spacing at smaller grafting densities for a given polymer length. It is not immediately clear what causes this behavior. We can think of three sources for the reduced basal spacing at a constant n_{CH_2}: **1.** A shift in the equilibrium position of polymers confined between solid layers. This can be verified by investigating the PMF of parallel polymer systems with end-to-end distance as the collective variable. **2.** The dependence of basal stiffness on polymer grafting density and **3.** A layer drift, which causes the polymers to tilt and the interlayer to collapse. What follows is a quantitative investigation of these hypotheses. Due to computational limitations, we only focus on 10 cases: $(\sigma_g, n_{CH_2}) \in \{1.3\text{nm}^{-2}, 2.6\text{nm}^{-2}\} \times \{2, 4, 6, 8, 10\}$. Samples with $\sigma_g = 1.3\text{nm}^{-2}$ are labeled LG (low grafting density) and those with $\sigma_g = 2.6\text{nm}^{-2}$ are labeled HG (high grafting density).

First, we construct a regular grid of parallel polymers with the same σ_g as in the composite samples (schematics in Figure 3.2a). The PMF for these samples with the collective variable being the distance between the layers can be calculated as explained in the methods section. The results for $n_{CH_2} = 4$ and two grafting densities are shown in Figure 3.2b (other lengths show similar behavior. See Supplementary Information Figure 1S for other cases). Intuitively, when we have higher polymer density, we expect inter-polymer steric repulsion to shift the

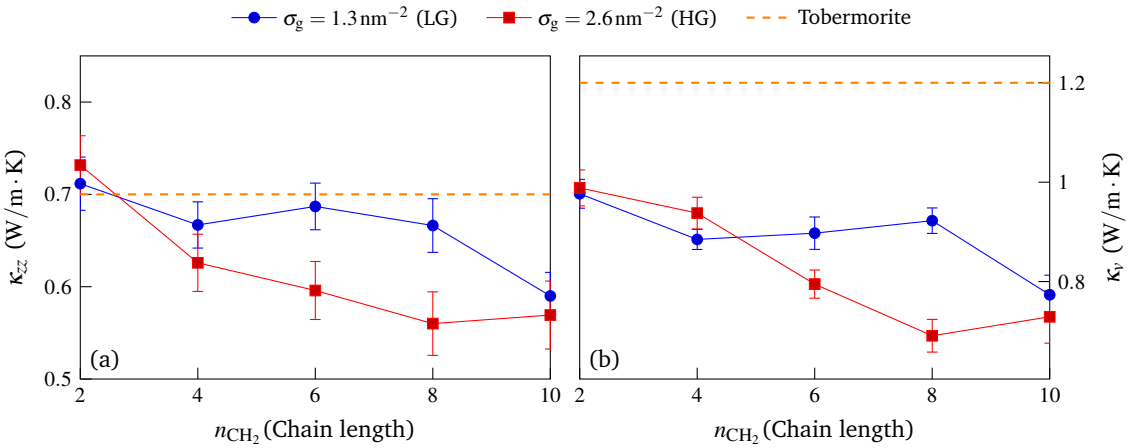

Figure 3.3: Reduction in thermal conductivity as longer chains are grafted into the interlayer. (a) cross-plane (z-direction) component of thermal conductivity. (b) Volumetric thermal conductivity. In this case, a significant reduction is observed for even the smallest chain length.

location of PMF minimum. However, at these values of σ_g, we only see a negligible shift, which means steric repulsion cannot be responsible for the observed decrease in the basal spacing at a constant n_{CH_2}. Moreover, if the PMF from the inorganic part is added to that of the polymer-only system, we still do not see any significant shift in the location of the minimum in the combined organic-inorganic PMF (Figure 3.2b). This is expected because at such a large basal spacing, the attractive ion correlation forces between the layers are weak[88, 89], as seen in the same figure. Also the difference in stiffness values near the minimum ($\partial_\lambda A(\lambda)$) between the two grafting densities is not large enough to cause the observed basal spacing. This means the reduced basal stiffness cannot be at the origins of reduced basal spacing at a given n_{CH_2}.

To investigate the impact of the relative lateral shift between solid layers, we calculate in-plane RMSD of bridging silicons for all samples (Figure 3.2c). It is clearly seen that there is a significant discrepancy between samples with high and low grafting densities at a constant polymer length. Since layers are cross-linked, the shift results in further tilting of the polymers, which entails a significant collapse of the interlayer spacing. But our simple model of parallel polymers on a regular grid is not able to capture this drift. So, we extract

the actual configuration of polymers from the interlayer of relaxed structures and repeat the PMF calculations with these disordered configurations. As shown in Figure 3.2d, there is a significant shift in the location of PMF minima, which is comparable to values reported earlier in Figure 3.1. This further confirms that the interlayer drift is the main reason behind the observed reduction in the basal spacing by varying grafting density. A more accurate demonstration would require the addition of sliding collective variables[88], which results in a 3D PMF in the collective variable configuration space. However, this approach currently remains computationally prohibitive.

Once properly relaxed hybrid organic-inorganic atomic structures are at hand, we can compute thermal conductivities using the Green-Kubo (GK) formalism for all samples. Here, we focus on κ_{zz} and the volumetric conductivity $\kappa_v = \frac{\kappa_{xx}+\kappa_{yy}+\kappa_{zz}}{3}$. As can be seen in Figure 3.3a, for $\sigma_{\mathrm{g}} = 1.3\mathrm{nm}^{-2}$ (LG), we only observe significant reduction in κ_{zz} for the longest chain length ($n_{\mathrm{CH_2}} = 10$). For $\sigma_{\mathrm{g}} = 2.6\ \mathrm{nm}^{-2}$ (HG), a steady reduction is observed up to $n_{\mathrm{CH_2}} = 8$. There seems to be a plateau after $n_{\mathrm{CH_2}} = 8$ which indicates a limit to control the conductivity based on $n_{\mathrm{CH_2}}$. For volumetric conductivity (Figure 3.3b), we have a reduction in conductivity of about 17% even for $n_{\mathrm{CH_2}} = 2$, irrespective of grafting density. $n_{\mathrm{CH_2}} = 10$ shows highest reduction for both κ_{zz} and κ_v (17% and 40%, respectively). We now focus on understanding the origins of the observed reduction in thermal conductivity.

As a first attempt, one might model thermal conductivity using a simple series model such as the following:

$$\frac{d_{\mathrm{total}}}{\kappa_{\mathrm{eff}}} = \sum_{\mathrm{layers}} \frac{d_i}{\kappa_i} + \sum_{\mathrm{interfaces}} \frac{1}{G_i} \tag{3.8}$$

where d is layer thickness and G is the interfacial thermal conductance. For TB layers, we assume $\kappa_{\mathrm{TB}} = 1.2\ \mathrm{W/m \cdot K}$ and $d_{\mathrm{TB}} = 11.2$ Å. For the organic layer, we take $\kappa_{\mathrm{ORG}} = 0.15\ \mathrm{W/m \cdot K}$ in our approximation based on values reported in the literature for amorphous

polymers ($0.1 \sim$ 0.2 W/m $\cdot$ K)[153]. Neglecting interface contributions, for (HG)$n_{\mathrm{CH_2}} = 6, 8$ we get $\kappa_{\mathrm{eff}} = 0.39, 0.33$ W/m $\cdot$ K, respectively, which is significantly lower than our GK calculations. Several contributing factors can be cited for the observed discrepancy. First, we expect the short polymer chains in our study, which are also covalently bonded to inorganic layers to have higher conductivity than bulk conductivity of amorphous polymers[134]. This is supported by previous investigations on the effect of bonding and cross-linking on thermal conductivity[64, 83]. Moreover, we used the bulk value of conductivity for the tobermorite layer, while the conductivity of a single layer is unknown. Bulk values can be further corrected due to size effects when they are used in continuum calculations[23], which further reduces κ_{TB} in Equation 3.8. The result is further reduction of κ_{eff} and further deviation from atomistic results. There are also interface effects between TB layers which is unknown when doing bulk calculations. The above discussion underlines the fact that simple continuum models are inadequate for our complex system at such small scales and more holistic modal analysis approaches are required to better understand the underlying physics of heat transport in organic-inorganic hybrids.

Figure 3.4 (a) shows vibrational density of states for TB, XTB at $n_{\mathrm{ch2}} = 8$ with high grafting (HG) and that of a single polymer. In a frequency range of 30$\sim$45 THz, we can see that polymer molecules have modes that are absent in TB. Hence, we can expect this modal mismatch to result in scattering at the interface between TB and the organic material, which manifests as reduced diffusivities as we show later on. In the literature, this vibrational mismatch is cited as the underlying reason for lower conductivity[41, 117]. This hypothesis can be further investigated by a full characterization of vibrational modes of the systems. Based on their spatial vector fields, these modes can be categorized into locons, diffusons or propagons[4]. To distinguish locons, we compute the modal participation ratio (PR) for all modes of each sample (a typical result is shown in Figure 3.4b). As discussed in the methods section, a cutoff value is needed (e.g. a value of 0.1 as used in some previous studies[130]). In this study, we use a more conservative value and modes with a PR smaller than 0.05 are

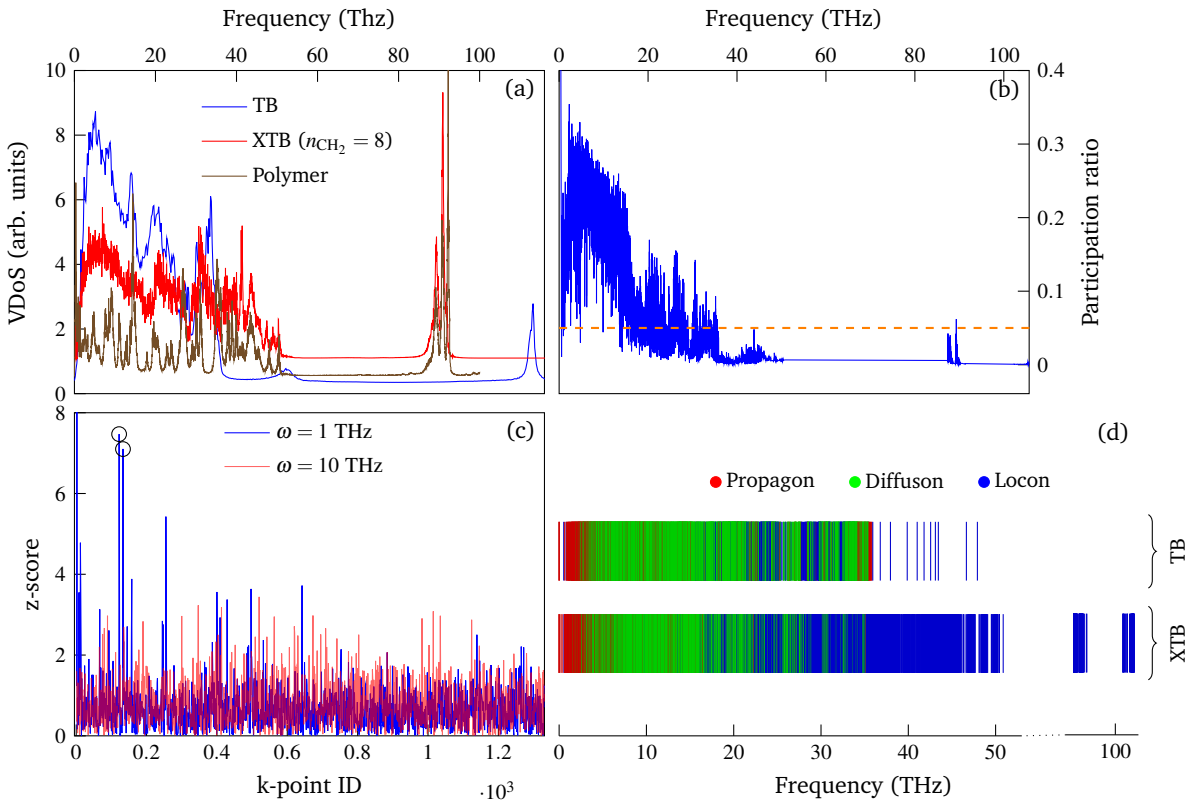

Figure 3.4: Modal analysis for tobermorite and cross-linked tobermorite (XTB) with $n_{CH_2} = 8$. (a) Vibrational density of states for tobermorite, polymer and XTB with $n_{CH_2} = 8$. Adding organic constituents introduces modes in an interval of about 30∼50 THz which is absent in tobermorite. This results in a vibrational mismatch between the organic and inorganic layers and leads to reduced mode diffusivities (b) Participation ratios are calculated for each mode. This data is used to distinguish locons (c) Results for spatial Fourier decomposition of two typical modes on the 3D Fourier basis. At lower frequencies, modes show dominant (outlier) amplitudes for particular wavevectors and are designated as propagons. The rest (except those already designated as locons) are labeled as diffusons (d) Full modal spectrum for TB and XTB with $n_{CH_2} = 8$. We can visually see the abundance of localized modes in the hybrid case compared to pristine tobermorite.

labeled as locons. Note that a higher value would result in higher conductivities. Moreover, the calculations are not sensitive to this limit since higher frequency modes (whose inclusion or exclusion is affected by the limit) already have small contributions to conductivity.

To distinguish propagating modes, we use equation 3.5 as described in the methods section. The results for two modes with low and medium frequencies are shown in Figure 3.4c. We see that modes with lower frequency (1 THz here) show marked peaks, which are absent

from modes with higher frequency (10 THz here). Regarding threshold value, as in the diffuson-locon limit, we choose a very conservative value of 6 for detecting propagons. This means that we have an outlier if the frequency amplitude has a negligible probability. In other words, we should have one or more sharp spikes in the data as in Figure 3.4c. After distinguishing localized and propagating modes, the remaining modes are labeled as diffusons. Figure 3.4d shows the full characterization spectrum for both TB and XTB. For TB, we calculated vibrational modes after introducing a defect in the system. However, due to crystallinity, a few anomalous propagating modes are observed at higher frequencies. Our results are compatible with previous findings for amorphous silicon, where propagating modes were observed even beyond the Ioffe-Regel threshold[130, 104]. From this spectrum, we can see that although a sharp difference is observed in the number of locons for TB and XTB, both have more or less the same number of propagons. But why do we have such a stark difference in the percentage of locons between TB and the composite system?

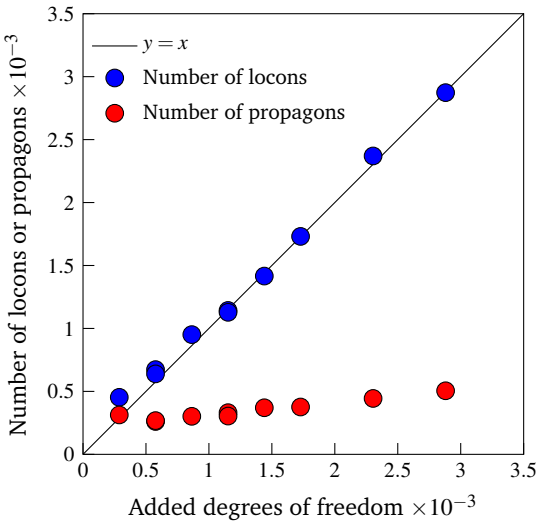

Figure 3.5: Number of locons and propagons in each sample as a function of added degrees of freedom. For locons, a linear relationship with a slope of 1 is observed which indicates modes added due to polymers are all locons. However, the number of propagons shows a negligible increase.

In Figure 3.5, we plot the number of locons and propagons as a function of degrees of freedom (DoFs) that are added to the TB structure (all added DoFs belong to the organic part).

Interestingly, we find that locons increase with a slope of almost 1, while the number of propagons shows a negligible increase. This is what was visually observed in Figure 3.4d as well. In a sense, one could say that although the number of modes available for thermal transport is more numerous in the hybrid system, those added DoFs are all localized and do not contribute to heat transport. So one can conclude that it is a change in the character of the same number of either diffusons or propagons that is lowering the thermal conductivity of the hybrid material.

To investigate this hypothesis quantitatively, we try to separate the diffusive part of conductivity (κ_v^d) from the propagative part (κ_v^p). This can be done by computing κ_v^d using Allen-Feldman theory as described in the methods section, which gives $\kappa_v^p = \kappa_v - \kappa_v^d$. Figure 3.6a shows that κ_v^d remarkably has the same decreasing trend as the total conductivity shown in Figure 3.3 and constitutes roughly 33$\sim$50% of κ_v. This value can be contrasted with the higher diffusive contribution in a more disordered system obtained by Zhou et al.[163]. However, as seen from Figure 3.6b, such trend is non-existent for $\kappa_v^p = \kappa_v - \kappa_v^d$. This points to the fact that the reduction in thermal conductivity mainly arises from a change in mode diffusivities. In the literature, this reduction is routinely attributed to "scattering of phonons at the interface" with the implicit assumption that the propagating modes are the only contributor. This is justifiable for multilayered crystalline materials with sharp interfaces (e.g. thermal interface conductance in Si/Ge superlattices[21]) studied in the literature. However, in our case the results show that the propagon contribution remains unchanged due to cross-linking and the reduction can only be attributed to diffusons. It further underlines the importance of full spectral analysis in complex hybrid materials.

Figure 3.6c shows mode diffusivities for a number of cross-linked models ($n_{\mathrm{CH_2}} = 2$ (LG), $n_{\mathrm{CH_2}} = 10$ (LG), $n_{\mathrm{CH_2}} = 2$ (HG), $n_{\mathrm{CH_2}} = 10$ (HG)) and the pristine TB. We see that overall, models with larger polymer length and higher grafting show lower diffusivities. These diffusivities can be used to compute cumulative κ_v^d for each model which is shown in

Figure 3.6d. Therein, we clearly see the reduced cumulative κ_v^d which arises as a result of hampered diffusivities. Combined with unchanged contribution from propagating modes, this quantitatively demonstrates that the reduction in heat conductivity can only be due to the reduced mode diffusivity of diffusons, which is in turn rooted in the modified interfaces in cross-linked samples compared to the pristine inorganic structure.

The procedures discussed in this chapter for separating propagating and diffusive contributions to thermal conductivity can just as well be applied to a range of materials (including materials with nanoconfined water[120]) to better understand the mechanisms underlying their heat transport. Such fundamental knowledge would ultimately assist with the design of new nanomaterials and nanoscale thermal processes. For instance, an interface is created when a nanoparticle is embossed through laser heating in a polymer matrix[138] which is amenable to a spectral analysis. Moreover, metal organic frameworks (MOFs) are a primary choice for water uptake at low relative humidity[19], as in design of energy efficient adsorption-based chillers[78].

It might be challenging to find biological applications for the particular prototype material used in our study. However, there are biological/biomimetic materials with similar characteristics amenable to thermal analysis. For instance, nacre is composed of platelets of aragonite separated by sheets of an organic matrix. Artificial analogs of nacre[142] can be synthesized with nanoscale platelet sizes which makes them ideal multifunctional materials where high fracture toughness and low thermal conductivity are simultaneously desired. In addition to nacre, layered double hydroxides (such as clays), which have similar structures to our system, can be used as controlled release systems for pesticides, genes and drugs among others[128]. Our experimental findings[106] show negligible swelling/shrinkage in these materials which can enhance the release of nanoconfined fluids without interlayer collapse. Chitosan-silane hybrids are another important class of materials which find applications in membranes, tissues or scaffolds[141].

Conclusions

The following concluding remarks summarize the new findings presented in this paper:

1. Bipodal organosilanes with different chain lengths can be used to cross-link nanoscale interfaces of layered inorganic materials such as tobermorite and phyllosilicates with different surface grafting densities. Higher grafting means larger basal spacing (at a constant polymer chain length) and in this paper, we have shown that the drift in the inorganic layer lies at the origins of this difference.

2. We show that organic cross-linking can reduce volumetric thermal conductivity as much as 40%, which is lower than values obtainable from pristine amorphous inorganic components.

3. A simple method for characterizing propagons was introduced. We show that the number of propagons is more or less unchanged as a function of carbon content. We also show, using participation ratio that the added organic modes due to cross-linking are all localized in nature.

4. By computing mode diffusivities for all modes of all samples, we show that a reduction in mode diffusivities in cross-linked systems is the main cause of the lower thermal conductivities observed in our organic-inorganic composites.

We envision that these findings can potentially pave the path toward designing a new generation of low-thermal conductivity insulating materials, which is the subject of our ongoing investigations. It is conceivable that our findings can have direct implications for designing thermally insulating hybrid materials with applications ranging from automotive to space industries.

From a computational prospective, this work opens up paths for future research. At larger

scales, the building blocks of the hybrid material studied (similar to pristine tobermorite) can be modeled as globules of several cross-linked layers. A coarse-grained model can be developed through free energy calculations and judicious choice of interaction potentials among these particles[87]. Once the meso-texture is at hand, upscaling of material properties can be achieved. Since we have already calculated thermal conductivity for the hybrid material at the nanoscale, a homogenization technique such as Mori-Tanaka theory can be used to compute conductivities at larger scales[17] based on computed porosities. Density, pore-size distribution and creep performance[105] are among other properties that can be studied using mesoscale models.

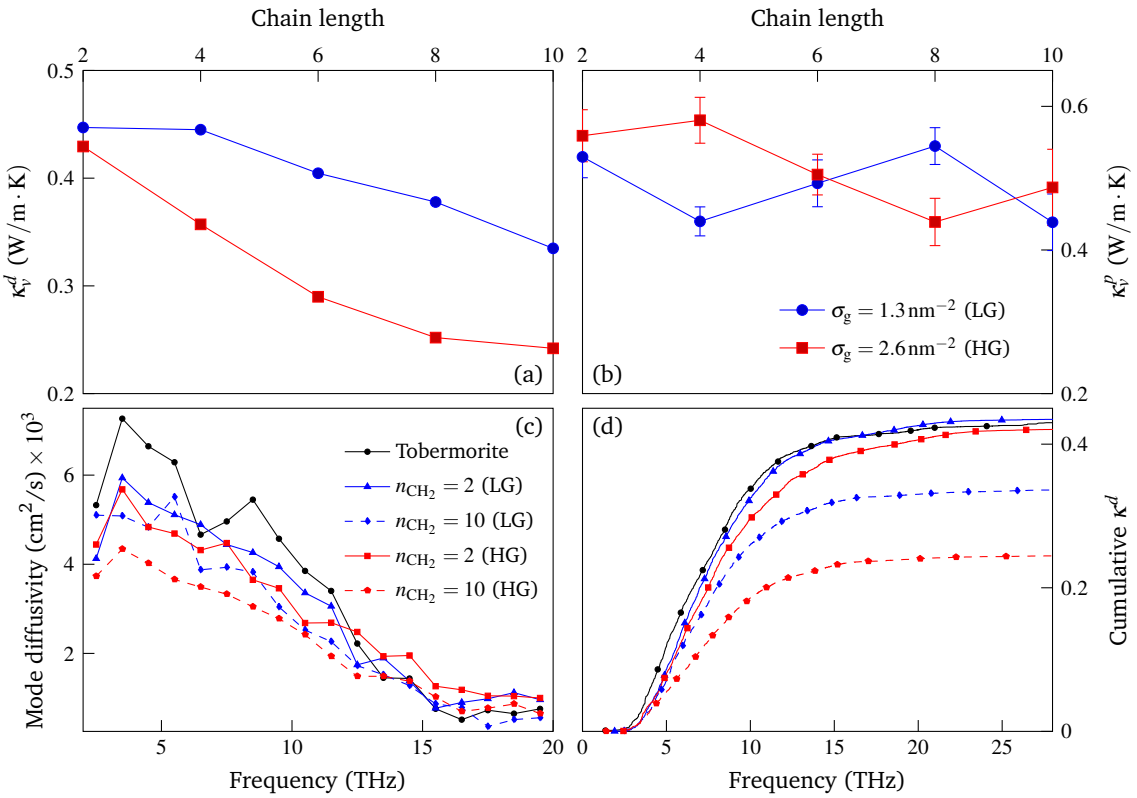

Figure 3.6: Decomposition of thermal conductivity into propagating and diffusive components and understanding origins of observed differences in diffusive contribution to thermal conductivity (a) The diffusive component computed using Allen-Feldman theory. The trend is similar to what was computed using Green-Kubo in this paper. (b) Propagon contribution obtained as $\kappa_v^p = \kappa_v - \kappa_v^d$. We see that the decreasong trend disappears. (c) Comparison of mode diffusivities for a number of cross-linked models and pristine TB. Overall, mode diffusivities show significant reduction due to cross-linking, where we have high grafting and long chain lengths. (d) Cumulative diffusive contribution to the thermal conductivity. For small chain length and low grafting percentage, we do not observe a significant change in κ^d compared to the pristine TB. The reduction is most significant for large chain lengths and high grafting percentages. See Figure 2S in Supplementary materials for other grafting and chain lengths. Lines in figures are guides for the eye.

Chapter 4

XC-S-H: A cross-linked calcium silicate hydrate for improved thermal and creep performance

4.1 Introduction

Most existing techniques to reduce thermal conductivity in construction materials utilize macroscopic features of the material. For instance, air voids or hollow glass microspheres can be introduced into the cement matrix to obtain concrete with lower thermal conductivity[69]. Creep performance can also be improved by incorporating various types of fiber in concrete (e.g. carpet fibers)[102, 162]. The question we want to address in this chapter is: is it possible to engineer the molecular structure of C-S-H gel to improve properties such as thermal and creep performance. In recent years, there has been significant research on the effect of Ca/Si ratio and atomic substitutions on C-S-H properties such as stiffness[119], fracture toughness[7] and creep[105] which can be categorized as the "inorganic approach". An example of this

strategy is the work of Pellenq and Gmira where bonding scheme of interstitial ions or surface charge density of C-S-H is leveraged to engineer gel cohesion. Although such techniques can potentially improve properties, however they still have limited application and remain mainly as an academic pursuit. Moreover, without considerable changes in the type and population of primary bonds existing in C-S-H molecular framework, the impact of such stoichiometric alterations may be very limited to none on certain properties. It was also recently shown that stoichiometric modifications of C-S-H have negligible effect on thermal conduction which can be attributed to their ineffectiveness in changing the nature of existing modes of conduction[121, 163].

An alternative approach in the molecular engineering of C-S-H emerges from the coupling of its inorganic framework with organic molecules. If successfully realized in cement environment, and complemented with optimum design of the mesostructure, such organic-inorganic hybrid C-S-H gels could potentially provide cement-based matrices with unique properties beyond their inorganic counterparts. For instance, recent investigations on clay minerals[82] show a 5-fold reduction in the thermal conductivity of organoclay nanolaminates compared to unmodified clay. However, the main question we should as is whether the nanoscale crosslinking of C-S-H with organic molecules in hydrating Portland cement systems is an attainable goal.

The problem of synthesis of organic-inorganic (O-I) C-S-H has drawn the attention of various research groups. In particular, the early works of Matsuyama and Young [91, 92], which were focused on the synthesis of C-S-H/polymer complexes, showed that the formation of stable hybrid complexes highly depends on the structure of the polymer and C-S-H template stoichiometry. Based primarily on the carbon content and X-ray diffraction measurements they concluded that: a) observed shift in 002 reflection is indicative of organic molecules intercalated in the interlayer space of C-S-H, b) the magnitude of change in the interlayer distance is governed by the type of organic molecule and Ca/Si ratio of the gel, and c) certain types of polymer can be also post-intercalated within already precipitated C-S-H product.

For example, for poly(methacrylic acid) (PMA) and poly(acrylic acid) (PAA) polymers, the maximum recorded expansion was about 1.5 nm and 1.2 nm, respectively. The authors suggested, that such large expansion is consistent with the intercalation of ≈2 monomer units in between the layers, and the high amount of polymer content in the complex is unlikely to be explained by the surface adsorption only. However, for small molecular weight polymers such as poly(vinyl alcohol) (PVA) the observed systematic expansion was significantly below the effective diameter of PVA molecule (0.45 nm) and does not seem to present strong evidence of intercalation.

In these studies, the possibility of interactions of C-S-H with various polymers was also considered. Following the study of 002 reflection shift measured on O-I C-S-H hybrids synthesized with neutral, anionic, and cationic molecules according to different synthesis methods, including direct precipitation, the experimental evidence pointed toward dominating role of surface adsorption rather than intercalation. Merlin et al.[93] hypothesized, that the high surface charge density of C-S-H layers effectively prevents polymers from entering the interlayer space, thus leaving adsorption as a primary mode of interaction. As a consequence, the texture of C-S-H / polymer hybrids resembles a "meso-composite", in which stacked C-S-H lamellae are confined by the surrounding polymer. Moreover, the adsorbed layer of a polymer affects the hydration state of C-S-H particles. Therefore, by retaining more water molecules within the interlayer space some C-S-H / polymer meso-composites may show the expansion of the basal distance as compared to polymer-free C-S-H submitted to the same mild drying. The dominant role of polymer adsorption over intercalation for various types of polymers was also suggested in [13, 61, 47]. For example, while working with hexadecyltrimethylammonium (HDTMA) molecules[13], a dipolar dephasing (DD) ^{1}3CP NMR experiment suggested the location of the methyl groups at the surface of the hydrate rather than incorporated within the layers. However, the possibility of intercalation could not be definitely ruled out either exposing the complexity of assessing interactions between organic molecules and non-stoichiometric solids like C-S-H.

The difficulties in overcoming the steric and entropic interactions, which tend to hinder the introduction of the organic molecules within the interlayer of C-S-H, seem to be reduced in sol-gel processing involving functionalized organometallics. By studying novel organic-inorganic gels, synthesized via sol-gel method using conventional organosilanes e.g. n-hexyltriethoxysilane (HTES), Minet et al.[95] showed a bi-layer type arrangement of the organic groups inside the interlayer. Moreover, the 002 shift and the length of the alkyl chain are positively correlated, and the molecular structure of such solids may be explained by smectite-type arrangement. However, given the constraint of only one Si-C bond in conventional organosilane, no direct chemical cross-linking in which opposite inorganic galleries are connected via continuous alkyl chain can be realized.

In this chapter, we explore the idea of direct chemical cross-linking of inorganic galleries of calcium-silicate-hydrates realized through hydrolysis and condensation of functionalized bis-alkoxysilanes (with two Si atoms covalently linked to C atoms at terminal sites of alkyl chain). First, we report relevant experimental findings of Moshiri et. al.[106] where organic-inorganic C-S-H gels were synthesized via sol-gel processing with organosilanes of alkyl [CH2]-n chain size ranging from 2 to 8. The samples were subjected to Inductively coupled plasma - optical emission spectrometry (ICP-OES) and X-ray powder diffraction to obtain clues about the nanoscale structure of the synthesized material. These experiments demonstrate that cross-linking of noscale galleries of C-S-H have been achieved.

Due to novelty of the material, little is known about its properties. Hence, our objective is to obtain an accurate atomistic model of the material which makes it possible to study its properties. First, the experimental findings are used in constructing the structure of the material for atomistic simulations. Density functional theory calculations are used to develop a quantum mechanically derived force field which can be used for molecular dynamics simulations. To achieve this goal, we have developed a novel fitting process that can be used to construct force fields for similar materials. Finally, thermal and creep properties of the

material are studied using the developed force field to demonstrate how it can be used in applications.

4.2 Experimental results[1]

In this section, we summarize experimental results that form the foundation of our modeling efforts later on. The sol-gel processing provides a unique opportunity for manipulation of the molecular structure of C-S-H with organometallic molecules. Measured concentrations of major elements (except carbon) constituting synthetic C-S-H and its organic hybrids are reported in Table 4.1. In most cases, Ca/Si atomic ratio of the precipitate is close to 1, which is the initial molar ratio of alcohol-based solutions used in organosilane hydrolysis. However, in the case of hex:C-S-H (chain length 6) gel the Ca/Si molar ratio is slightly below the target value designed in the experiment suggesting close to but not optimum synthesis conditions have been achieved. Finally, the highest uptake of alkaline ion Na+ is recorded for reference C-S-H gel, around 1%, while in hybrid gels it is significantly lower.

Table 4.1: Chemical composition of synthesized gels as measured with ICP-OES.

Gel type	Ca (wt%)	Si (wt%)	Na (wt%)	Ca (mol)	Si (mol)	Ca/Si
C-S-H	24.17 ± 1.07	16.65 ± 0.91	1.16 ± 0.15	0.60 ± 0.03	0.59 ± 0.03	1.02 ± 0.03
hex:C-S-H	18.72 ± 1.48	13.92 ± 1.02	0.09 ± 0.02	0.47 ± 0.04	0.50 ± 0.04	0.94 ± 0.08
oct:C-S-H	15.90 ± 0.72	10.85 ± 0.24	0.27 ± 0.01	0.40 ± 0.02	0.39 ± 0.01	1.03 ± 0.02

The first direct evidence of successful incorporation of organometallic molecules into the molecular structure of synthesized gel is provided by X-ray powder diffraction performed in the low 2θ range (Figure 4.1), which encompasses the basal reflection d_{002} of C-S-H[125].

It is observed that incorporation of longer chain organosilanes increases the interlayer spacing relative to C-S-H d_{002} reflection located at ≈12.7 Å (≈7° 2θ). This effect is especially evident for hex:C-S-H and oct:C-S-H. Thus, a stratified molecular structure with long-range order in

[1]This section was adapted from Moshiri et. al[106]

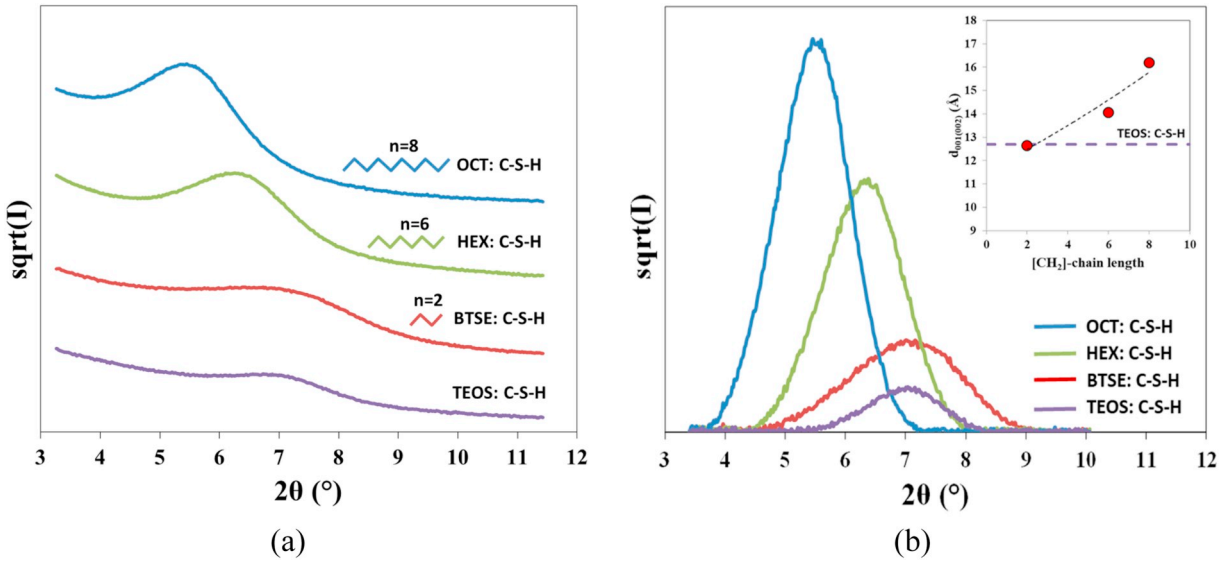

Figure 4.1: Basal reflection position in the C-S-H gels modified with BIS-organosilane molecules: (a) raw X-ray diffraction spectra, (b) basal diffraction peaks isolated after background removal, change in basal distance vs. $[CH_2]$ – chain length presented on the inset. Powders dried for 24h at 50°C under vacuum.

the c-direction has been established with possible condensation of silica tetrahedron on the Ca polyhedron layers. A similar trend in the expansion on the unit cell was reported by Minet et al.[95] for organosilicate hybrids incorporating silanes with only one Si-C bond and non-hydrolyzable organic moiety, e.g. n-hexyltriethoxysilane (HTES). On the contrary, the basal reflection position in BTSE (1,2-Bis(triethoxysilyl)ethane) modified C-S-H remains unchanged relative to C-S-H, suggesting that small size organic molecules can be accommodated within the interlayer space without causing dilation along c crystal axis. In addition, such small molecules seem to lead to a lower degree of crystallinity and/or crystallite size as indicated by the largest broadening of the basal peak.

The change in the interlayer distance upon continuous dehydration is another important point worth consideration here. By heating tobermorite 14 Å, a reduction in the interlayer distance is obtained through the progressive dehydration process [159]. Likewise, the basal spacing of quasi-crystalline C-S-H shrinks upon losing the interlayer water [144]. For C-S-H with $CaO/SiO_2 \approx 1$, the contraction from $\approx$ 13Å (mild drying conditions) to $\approx$ 11Å (harsh drying)

has been reported [90]. Similar behavior is observed in the baseline C-S-H sample (Figure 4.2), where the contraction of d_{002} from 12.6 Å($\approx 7^\circ$ 2θ) to 10.8 Å($\approx 8^\circ$ 2θ) is recorded upon changing drying conditions from 50 °C to 105 °C. However, a very contrasting phenomenon is displayed by organic-inorganic C-S-H hybrids. As revealed by X-ray data (Figure 4.2), the interlayer spacing in these materials is not affected by changing the drying conditions from mild to more severe, indicating no shrinkage along c-direction. Such retention of the basal distance can be realized by the cross-linking of Ca-galleries with alkyl chains, thus providing another experimental evidence of the successful hybridization of calcium-silicate-hydrate. It must be noted, the possibility of organosilane molecules present in the different conformational states within the interlayer space cannot be excluded at the current stage and requires further investigation.

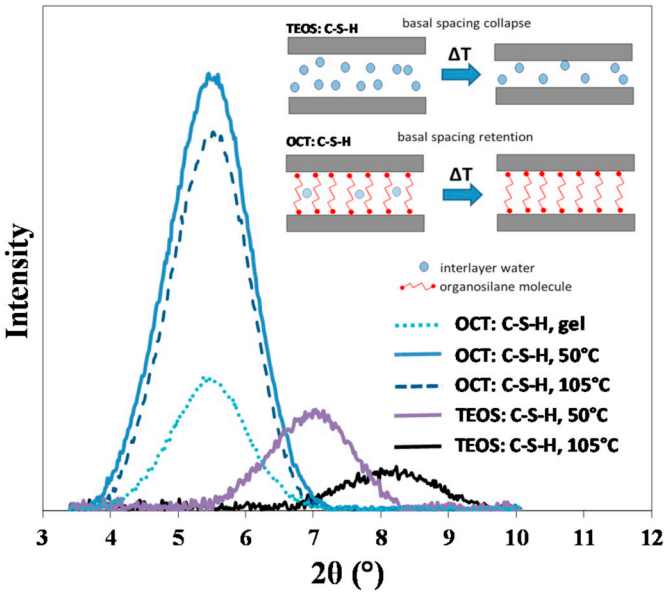

Figure 4.2: Effect of dehydration on the interlayer distance in the TEOS:C-S-H and oct:C-S-H

The incorporation of the organic molecules within the molecular framework of C-S-H hybrids has also important implications for the structural order in a-b plane. Accordingly, as presented in Figure 4.3a the reference TEOS:C-S-H (Tetraethyl orthosilicate) sample exhibits a few and broad diffraction maxima located at 5.34 Å, 3.04 Å, 2.81 Å, 2.06 Å, 1.83 Å, and 1.67 Å, many of which are hk0 type. This is in line with the commonly observed set of reflections

systematically observed in patterns from synthetic and OPC based C-S-H [44, 43]. Of particular importance is the triplet 3.04 Å, 2.81 Å, 1.83 Å, which corresponds to coherent scattering from regularly arranged atomic planes, e.g. calcium in the polyhedral calcium layer (Figure 4.3b).

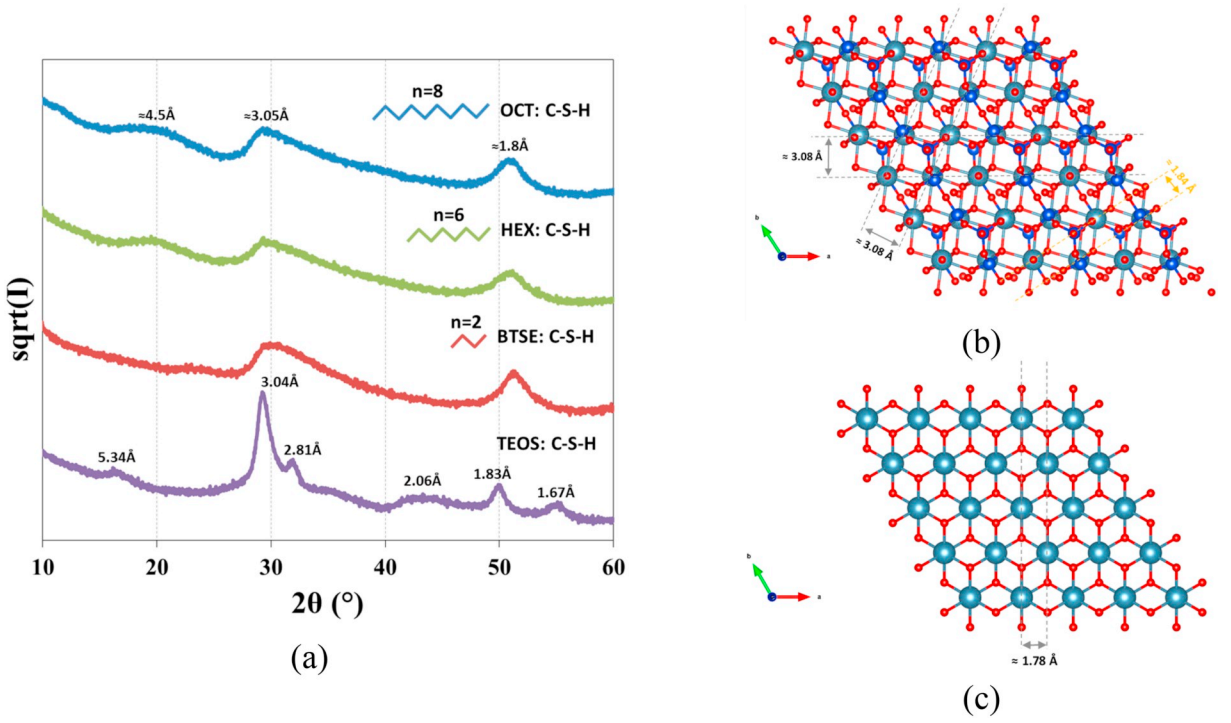

Figure 4.3: a) Global X-ray diffraction spectra of organosilane-modified gels and TEOS:C-S-H b)Atomic structure of 11 Åtobermorite, monoclinic polytype, after Merlino et al. [94] c) structure of portlandite

A quite different picture is obtained on the hybrids of C-S-H gel synthesized with organosilanes. The main differences include: (a) reduced number of diffraction events corresponding to coherent X-ray scattering in a-b plane, (b) increased broadening in which maxima tend to take the form of wide bands, and (c) clear asymmetry of the main band centered at ≈30°deg. 2θ angle. BTSE, hex and oct: C-S-H gels show a common pattern with the broad bands located at ≈3.05 Åand ≈1.8 Å. However, the band located at ≈4.5 Åis missing in the BTSE: C-S-H, which was synthesized using the shortest carbon chain organosilane, n = 2. Based on these results, it is apparent that the molecular structure of hybrid C-S-H gels shows a lower degree of ordering in a-b plane as compared to their inorganic counterpart.

Given the XRD observations, it is worth asking whether some conclusions can be reached regarding the possible stratification of the Ca atoms within the central layer of C-S-H hybrids. By analogy to tobermorite, C-S-H comprises of "stratified" calcium polyhedra, which are displaced along c axis by ≈2 Årelative to each other (Figure 4.4a). Depending on the crystal, the unit cell has an orthorhombic or monoclinic character. On the contrary, the Ca atoms in portlandite structure form planar sheets (see Figures 4.3c and 4.4b) and the unit cell is hexagonal[126]. A typical feature of the hexagonal unit cell is the ratio d_{100} /d_{110}, which has theoretical value of $\sqrt{3}$. If the two main reflections observed in the hybrid gels are assigned to 100 and 110 planes, respectively, their d-spacing ratio is around 1.704 for oct: and hex: C-S-H gels, which is close to the theoretical value. However, in BTSE: C-S-H gel this ratio is significantly lower, 1.687. This observation, together with observed trends in the basal reflection (Figure 4.1b), suggests a nanocrystalline turbostratic structure of hybrid gels in which randomly stacked hexagonal layers of Ca-polyhedra display systematic random translations or/and rotations between adjacent sheets[45].

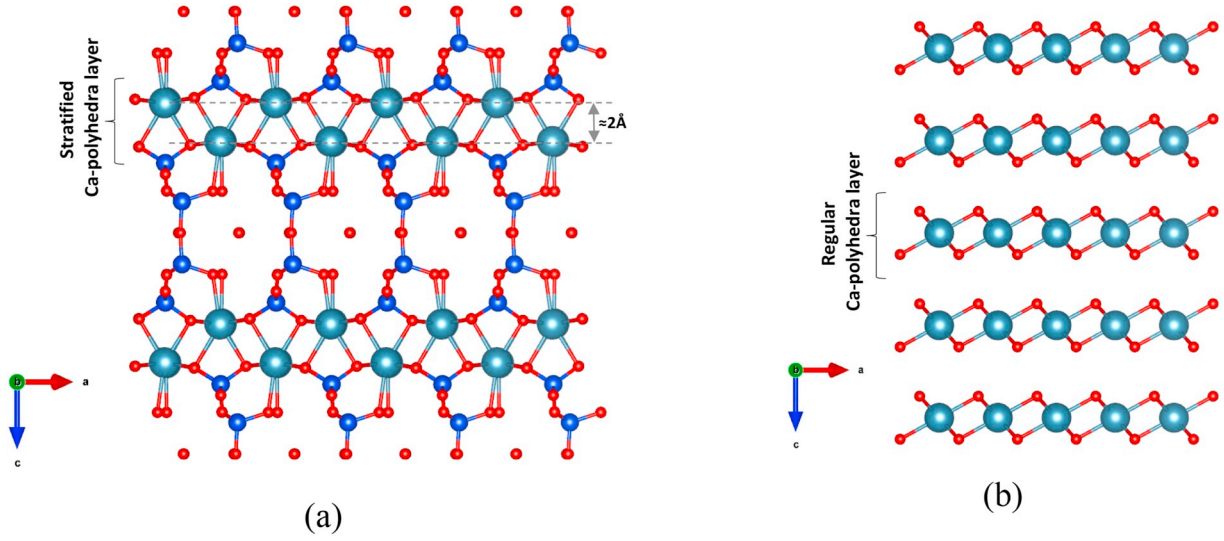

Figure 4.4: Projections of the atomic structure on the surface normal to b unit cell vector: (a) 11 Å tobermorite (monoclinic type, Merlino et al. [44]) comprising a stratified layer of Ca polyhedra along c, (b) portlandite with uniform Ca polyhedral layer.

The in-plane hexagonal symmetry and turbostratism of (Al, Mg, Ca)-alkylsilicates, derived

from the sol-gel processing of trialkoxysilane with n-alkyl functionality, has been also suggested by Ukrainczyk et al.[147] and Minet et al.[95]. By using the analogy with 2:1 trioctahedral Mg-phyllosilicates, e.g. smectite, the latter authors estimated a Ca-Ca distance of 0.351 $\pm$ 0.005 nm, which is close to the $d_{Ca\text{-}Ca}$ found in the brucite-like layers of portlandite.

4.3 Atomic structure

Based on experimental information available to us from the previous section, we can construct an atomic model of the material which makes it possible to further study the material via simulations. We start by constructing a supercell of portlandite using the following transformation matrix:

$$\mathbf{T} = \begin{bmatrix} 2 & 0 & 0 \\ 1 & 2 & 0 \\ 0 & 0 & 1 \end{bmatrix} \tag{4.1}$$

which gives an orthogonal unit cell with parameters $a = 7.185$Å, $b = 6.22$Å, $c = 4.905$Å, $\alpha = 90$, $\beta = 90$ and $\gamma = 90$. Next, dipodal organosilanes are grafted on both surfaces of portlandite galleries to achieve cross-linking. In this study we focus on chain lengths $n = 4, 6, \text{and} 8$. To graft the silicate end of the polymers to the surfaces, the interlayer space required is estimated based on expected polymer length. Cell height is set to 11.5Å, 14Å and 16.5Å for lengths 4, 6 and 8 respectively. This arrangement results in a structure that is close to an energy minimum and can be optimized with density functional theory calculations.

4.4 Dispersion-corrected DFT calculations

Periodic GGA-DFT calculations were carried out using vasp simulation package[71]. The energy cutoff was set to 600 eV for the plane wave basis set. The projector wave method[15] is used in our calculations. Moreover, Grimme's D2 method[46] was used to account for dispersive interactions between atomic species in the system. Based on the system size, a $2 \times 2 \times 1$ grid of kpoints was adopted to sample the Brillouin zone. After initial setup, the system with smallest chain length ($n = 4$) is energetically minimized for both atomic and cell degrees of freedom (DoF) using the conjugate gradient optimizer as implemented in vasp. Although the initial atomic configuration created based on experimental data should be close to an energy minimum, we found that the optimization needs to be carried out in stages for the system to settle into a high quality minimum. After some trial and error, the following scheme was adopted:

1. Layers are held fixed (including silicate tetrahedra). No cell DoF involved. CH_2 in the interlayer are relaxed.
2. Similar to previous step, but all carbon and hydrogen atoms are free
3. All ions are free, but still no cell DoF.
4. All ions and cell DoFs are used for optimization.

After the DFT-optimized structure for tet:C-S-H is at hand, we can simply expand the interlayer in the structure and add $[CH]_2$ blocks to construct hex and oct:C-S-H models. This approach provides better starting points for DFT optimization of these latter structures. The final DFT-optimized structures for the three models can be seen in Figure 4.5.

Besides the optimized structure, the DFT calculations can also provide lumped atomic charges and elastic constants for the three samples which are essential for developing the

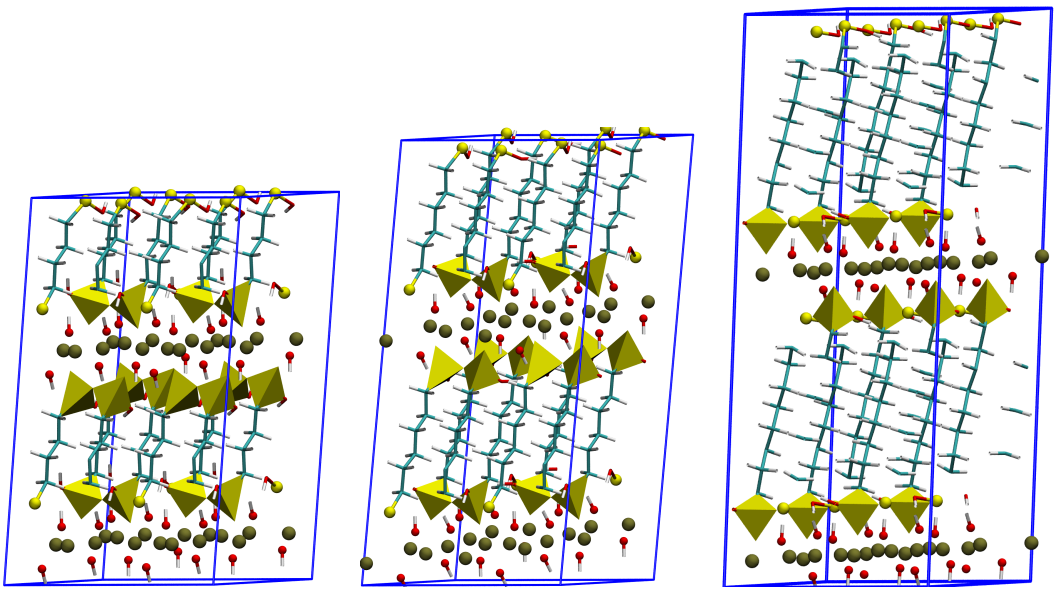

(a) (b) (c)

Figure 4.5: DFT-optimized atomic structure of XCSH. Red, cyan, white, yellow and tan represent Oxygen, carbon, hydrogen and silicon respectively and the chain lengths are a) n=4 b) n=6 and c) n=8

force field later on. Charges are computed from electronic density of the optimized hex:C-S-H system using Density Derived Electrostatic and Chemical (DDEC6) charge partitioning technique and its related code (chargemol) developed by Manz group[85]. Elastic constants are calculated using finite difference by applying a small distortion to the simulation box and performing a self consistent electronic relaxation at the deformed state. If we define cell matrix as $\mathbf{h} = [\mathbf{a}\ \mathbf{b}\ \mathbf{c}]$ where $\mathbf{a}, \mathbf{b}, \mathbf{c}$ are column cell vectors, the small strain tensor can be defined as[110]:

$$\varepsilon = \frac{\mathbf{1}}{\mathbf{2}}(\mathbf{h}\mathbf{h}_\mathbf{0}^{-\mathbf{1}} + \mathbf{h}^{-\mathbf{T}}\mathbf{h}^{\mathbf{T}}) - \mathbf{I} \tag{4.2}$$

where $\mathbf{h}_0$ and $\mathbf{h}$ are the initial and deformed cell matrices. Since we have $\sigma_{ij} = C_{ijkl}\varepsilon_{kl}$, we can compute each component of the elastic tensor if we apply a deformation which gives a

single non-zero strain component ($\mathbf{h} = \mathbf{M}\mathbf{h}_0$). For example for the x direction we have:

$$\mathbf{h} = \begin{bmatrix} 1 + d\varepsilon_{xx} & 0 & 0 \\ 0 & 1 & 0 \\ 0 & 0 & 1 \end{bmatrix} \times \mathbf{h}_0 \xrightarrow{\text{Eq 4.2}} \varepsilon = \begin{bmatrix} d\varepsilon_{xx} & 0 & 0 \\ 0 & 0 & 0 \\ 0 & 0 & 0 \end{bmatrix} \tag{4.3}$$

where $d\varepsilon_{xx}$ is the strain increment needed for finite differnce calculations. By repeating the process for all components, the elastic tensor can be computed. The completely anisotropic elastic tensor has 21 distinct components. Since we are dealing with a layered material, we assume transverse isotropy which reduces non-zero elements to only 5. However DFT results later on demonstrate an in-plane anisotropy which we take into account by including a 6th constant namely C_{22} in our fitting process. In voigt notation we have:

$$\begin{bmatrix} \sigma_{xx} \\ \sigma_{yy} \\ \sigma_{zz} \\ \sigma_{yz} \\ \sigma_{xz} \\ \sigma_{xy} \end{bmatrix} = \begin{bmatrix} C_{11} & C_{12} & C_{13} & 0 & 0 & 0 \\ C_{12} & C_{22} & C_{13} & 0 & 0 & 0 \\ C_{13} & C_{13} & C_{33} & 0 & 0 & 0 \\ 0 & 0 & 0 & C_{44} & 0 & 0 \\ 0 & 0 & 0 & 0 & C_{44} & 0 \\ 0 & 0 & 0 & 0 & 0 & (C_{11} - C_{12})/2 \end{bmatrix} \begin{bmatrix} \varepsilon_{xx} \\ \varepsilon_{yy} \\ \varepsilon_{zz} \\ \varepsilon_{yz} \\ \varepsilon_{xz} \\ \varepsilon_{xy} \end{bmatrix} \tag{4.4}$$

4.5 XCSHFF: A quantum mechanically derived force field for simulating cross-linked calcium silicate hydrates

To train a force field for molecular dynamics simulations, we first need to decide a functional form for the energy of the system and then adopt a strategy for fitting the parameters. To be able to incorporate existing knowledge from well-developed force fields that apply to systems

related to XC-S-H, we adopt the following functional form:

$$U = \sum_{\text{bonds}} k_b(r - r_0)^2 + \sum_{\text{angles}} k_a(\theta - \theta_0)^2 + \sum_{\text{dihedrals}} k_d(1 + cos(n\phi)) + \sum_{\text{pairs}} 4\varepsilon \left[\left(\frac{\sigma}{r}\right)^{12} - \left(\frac{\sigma}{r}\right)^{6} \right] + U_{\text{elec}} \quad (4.5)$$

where U_{elec} is the electrostatic contribution to energy. This expression contains 7 parameters that should be computed by fitting to observables obtained from DFT calculations. Now we focus on a strategy for computing these parameters.

The fitting process can be significantly facilitated if we can find parameters from the literature which can initialize the fitting process. ClayFF[26] and CVFF[28] force fields perform exceptionally well for portlandite and organic materials respectively. So we extract relevant parameters from these force fields to initialize $k_b, k_a, k_d, \varepsilon$ and σ and atomic charges. Based on their respective environments, the particles in our systems are divided into 12 atom types. These types and their initial values can be seen in table 4.2.

Table 4.2: Atom types, DDEC6 charges and paramer initialization based on ClayFF and CVFF

Atom type	Initial charges (e)	DDEC6 charges (e)	ϵ (kcal/mol)	σ(Å)
calcium (Ca)	1.05	1.464	5.0298e-06	5.5667
silicon (Si)	1.425	1.453	1.8405e-06	3.302
hydroxyl oxygen 1 (Oh1)	-0.95	-1.061	0.1554	3.1655
silicate oxygen 3 (Oh2)	-0.95	-0.805	0.1554	3.1655
silicate oxygen 2 (Om)	-0.95	-0.881	0.1554	3.1655
silicate oxygen 1 (Os)	-0.95	-1.050	0.1554	3.1655
Layer hydrogen (Ho)	0.425	0.374	0.0	0.0
Silicate hydrogen (Hs)	0.425	0.386	0.0	0.0
hydrogen 1 (Hc)	0.1	0.065	0.038	2.4500
hydrogen 2 (Ha)	0.1	0.141	0.0	0.0
aliphatic carbon (C)	-0.2	-0.131	0.039	3.8754
silicate carbon (Cs)	-0.2	-0.603	0.039	3.8754

The initial parameters result in large forces on atoms in the DFT-optimized structure which

means the desired minimum is vastly different from what we are getting from the combined ClayFF-CVFF force field. Consequently, an optimization attempt using initial parameters results in significant structural deviations from DFT restults (see Tables 4.3 and 4.4). As a first step, we substitute charges with those calculated based on DDEC6 as can be seen in table 4.2. These values are in most cases compatible with the initially assigned charges. However, in some cases such as carbon attached to silicons on the surface, the charge is significantly improved compared to those provided from ClayFF and CVFF. Moreover, since we have considered a larger number of atom types, charge assignment based on DDEC6 is able to distinguish between these types. Next, we try to adjust the initial parameters to minimize the sum of squares of force components on the atoms as expressed in the following equation:

$$F = \sum_{\text{DoFs}} f_i^2 \tag{4.6}$$

where f_i is the corresponding force on a degree of freedom (DoF). Since the initial parameters have reasonable physical significance, we don't want to deviate too much from them. We adopt a genetic algorithm (GA) optimizer as implemented in gulp[38] and explore an interval of $\pm 20\%$ around the initial parameters with a fine discretization of 2^10. The result of this optimization is not guaranteed to be the global optimum but we obtain a set of parameters that give much smaller forces on the DFT-optimized structure and hence a subsequent molecular optimization using the updated force field results in good agreement with structural DFT observables.

Since we plan to use the force field to study thermal and mechanical properties later on, we need to include second order properties in the set of observables obtained from DFT calculations. We choose the 5 elastic constants for a transversely isotropic material plus C_{22} as shown in Equation 4.4. We adopt a local optimization strategy which attempts to

minimize the following sum:

$$F_{\text{elast}} = \sum_{\text{i,j}} (C_{\text{ij}}^{\text{MM}} - C_{\text{ij}}^{\text{DFT}})^2 \tag{4.7}$$

where $(i, j) \in (1,1), (2,2), (3,3), (4,4), (1,2), (1,3)$. The challenge here is that elastic properties need to be calculated at a local minimum and we need a full optimization after each modification step in parameters. Explained in more detail, in this stage, each of the bonding and LJ parameters are incremented about the initial value and an optimization is performed (increments range from 0.1$\sim$1%). The parameter increment that gives the most reduction in F_{elast} is accepted. The process is repeated until no parameter change results in a lower values for F_{elast}. An additional criteria for accepting a change is that cell parameters and elastic constants should not exceed the assigned error tolerance. We set an error tolerance of 8% for cell parameters and 20% for elastic constants. Note that elastic constants are fit to DFT results for hex:C-S-H and the transferability of the obtained parameters is checked by comparing DFT resutls for tet:C-S-H and oct:C-S-H. The developed strategy for optimization can be seen in Figure 4.6.

With the set of parameters at hand, we can investigate the performance of the force field by comparing various characteristics of tet,hex and oct: C-S-H with DFT results and experiments (in case data is available). After fully relaxing the structures using the developed force field, we can immediately extract structural data i.e. cell parameters. As can be seen in Table 4.3, the average error for the initial ClayFF-CVFF parameters for hex:C-S-H is 14.6% which is reduced to only 2.6% after the fitting process. Note that the fitting strategy developed in this chapter, allows for prescribing a desired error for cell parameters. However, a smaller error means a more computationally costly and challenging fitting process. Note that hex:C-S-H has the smallest error as expected since this is the structure we used for fitting. The force field performs remarkably well for both tet and oct:C-S-H with average errors of 2.7% and 4.4% which shows the transferability of the force field to other chain lengths.

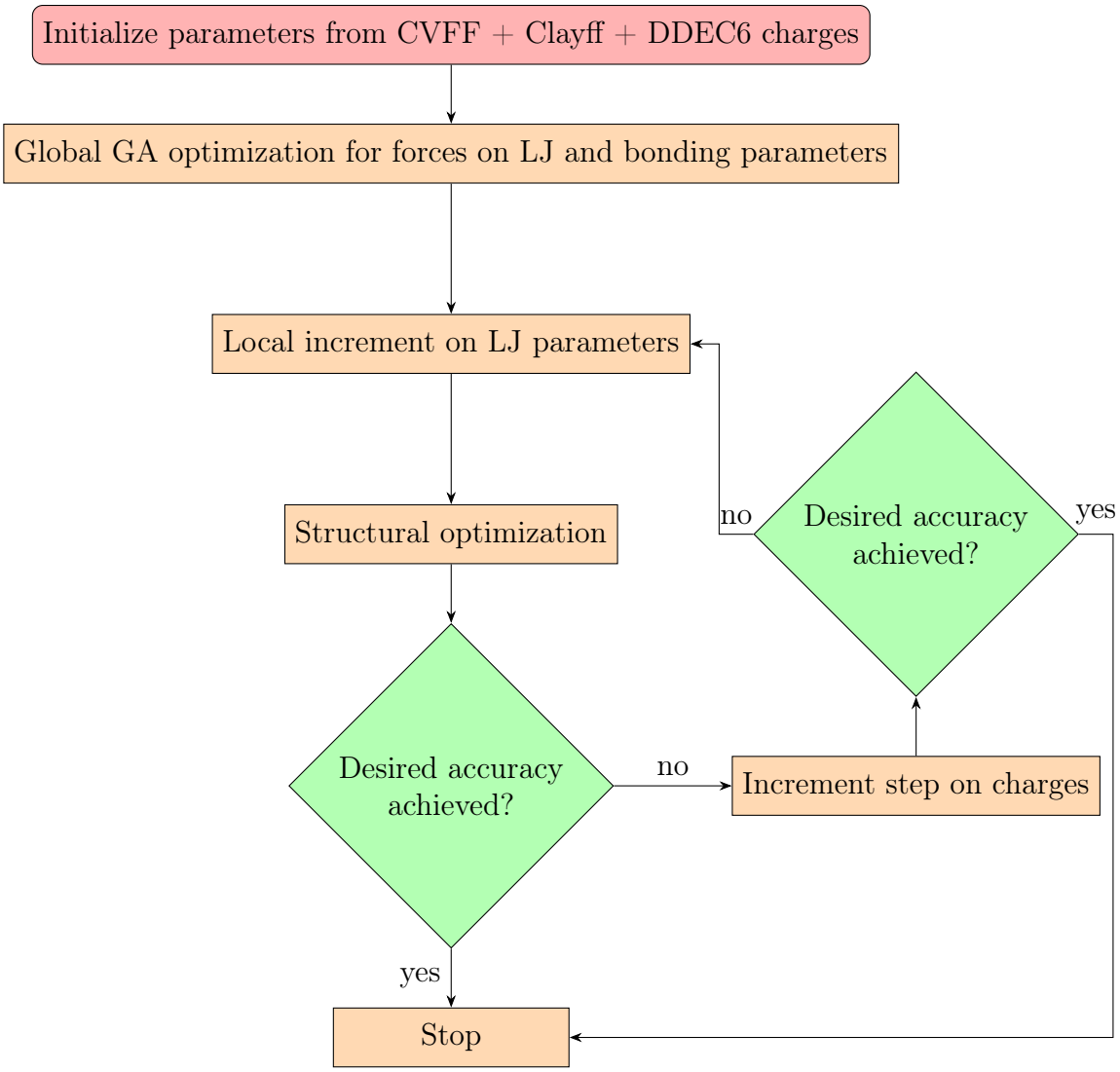

Figure 4.6: Flowchart demonstrating the strategy developed for force field parametrization

Regarding elastic constants, the main quantity used for measuring quality of the fit is the distance between the DFT and FF elastic tensors. In this study, we use the Euclidean measure of distance which allows us to also compare the results with similar computations on Tobermorite 11 Åreported by Shahsavari et. al[132]. The normalized Euclidean distance is defined as:

$$\frac{d_E(\mathbf{C}_{\mathrm{DFT}}, \mathbf{C}_{\mathrm{FF}})}{|\mathbf{C}_{\mathrm{DFT}}|} \tag{4.8}$$

Table 4.3: Cell parameters based on both DFT and foce field calculations. The values are compared with initial ClayFF-CVFF parameters

Sample	Method	a	b	c	α	β	γ	Average error(%)
	DFT	6.86	6.94	11.59	92.11	83.54	89.22	
tet:C-S-H	$FF_{initial}$	4.99	7.95	14.17	74.81	69.62	87.40	16.9
	FF	6.90	7.48	14.71	91.89	79.59	90.41	2.7
	DFT	6.80	6.98	13.97	90.84	79.16	90.96	
hex:C-S-H	$FF_{initial}$	5.26	7.44	16.92	79.79	72.59	76.12	14.6
	FF	6.90	7.4	14.7	91.8	79.5	90.41	2.6
	DFT	6.71	6.99	16.13	92.40	71.96	91.09	
oct:C-S-H	$FF_{initial}$	5.03	7.63	19.65	95.04	72.95	90.56	10.8
	FF	6.88	7.53	17.32	92.81	76.37	90.49	4.4

We compute a distance of 0.09 for hex:C-S-H which compare well with 0.11 reported for CSHFF for Tobermorite 11 Å[132]. Note that the level of accuracy for XC-S-H is more challenging to achieve compared to Tobermorite since we are not dealing with a well-defined crystal in the case of the hybrid material. The average error for hex:C-S-H is 10% which is about a 4-fold improvement compared to the initial error of 39%. This might seem a high value compared to the error in cell parameters, but we should note that elastic parameters are a second order property of the material and the fitting process is roughly an order of magnitude more costly than fitting for cell parameters alone due to the optimizations involved in each step. However, in future developments if a more strict tolerance is required, the fitting procedure developed herein allows the user to prescribe the level of accuracy desired.

We now turn to experimental data which we can compare to both DFT and FF results. The main data we have are basal spacing extracted from X-ray diffraction results (Figure 4.1 and desnity. Table 4.5 provides the computed values for basal spacing and density from DFT and FF calculations. The FF values can be compared to DFT results to measure the performance of the force field and DFT results can be compared to experiments to assess how realistic the

Table 4.4: Elastic constants (GPa) computed by finite difference for both DFT and molecular mechanics based on the developed force field (FF). Values are also compared with results based on initial ClayFF-CVFF parameters.

Sample	Method	C_{11}	C_{22}	C_{33}	C_{44}	C_{12}	C_{13}	Average error(%)*	Euclidean distance
tet:C-S-H	DFT	48.53	60.91	99.69	13.26	14.37	22.18		
	$FF_{initial}$	32.58	50.29	10.12	1.87	13.84	5.49	50.8	1.5
	FF	45.02	49.61	84.41	11.00	9.95	21.61	15	0.13
hex:C-S-H	DFT	36.10	40.03	88.40	4.13	6.12	16.80		
	$FF_{initial}$	37.08	38.86	12.34	4.13	10.85	5.90	39.0	1.3
	FF	37.18	43.55	81.28	7.51	7.34	20.23	10	0.09
oct:C-S-H	DFT	33.58	42.59	88.31	5.95	9.87	17.67		
	$FF_{initial}$	42.32	45.02	12.20	2.55	9.87	6.15	29.4	1.2
	FF	31.33	37.09	70.23	4.94	5.03	17.91	10	0.17

*Values smaller than 5 GPa are ignored

overall model is. Table 4.6 shows that DFT results agree exceptionally well with experimental results which demonstrates the adequacy of the model adopted as far as density and basal spacing are concerned. The force field shows expansion of the box within 5% in all directions which results in some significant deviation in density. If desired, this error can be reduced by incorporating density as an observable in the fitting process.

Table 4.5: Basal spacing and Density

Quantity	Method	tet:C-S-H	hex:C-S-H	oct:C-S-H
Basal spacing (Å)	Exp.	-	14.0	16.2
	DFT	11.56	13.90	15.94
	FF	12.09	14.49	16.80
Density (g/m^3)	Exp.	-	1.71	1.58
	DFT	1.81	1.71	1.68
	FF	1.71	1.52	1.48

Table 4.6: Error in basal spacing and density (%). DFT results show excellent accuracy when compared to experimental data. Quantities calculated with the developed force field are also compared to DFT results.

Quantity	Type	tet:C-S-H	hex:C-S-H	oct:C-S-H
Basal spacing	DFT wrt Exp.	-	0.7	1.5
	FF wrt DFT	4.5	4.2	5.3
Density	DFT wrt Exp.	-	0.0	6.0
	FF wrt DFT	5.5	11.7	11.9

4.6 Average elastic properties

The elastic tensors can also be compared by condensing the components into quasi-isotropic properties, namely bulk and shear moduli. The most common approach is based on the techniques developed nearly 100 years ago by Voigt[151] and Reuss[123] which respectively provide an upper and lower bound for bulk moduli, K, and shear modulus, G. The arithmetic mean of Voigt and Reuss bounds is known as the Voigt–Reuss–Hill (VRH) approximation[50] which is classically used in mineralogy to estimate the elastic constants corresponding to a random polycrystal. The Voigt upper limits can be calculated as:

$$K^{\text{Voigt}} = \frac{1}{9}\left(C_{11} + C_{22} + C_{33} + 2\left(C_{12} + C_{13} + C_{23}\right)\right) \tag{4.9}$$

$$G^{\text{Voigt}} = \frac{1}{15}\left(C_{11} + C_{22} + C_{33} + 3\left(C_{44} + C_{55} + C_{66}\right) - C_{12} - C_{23} - C_{13}\right) \tag{4.10}$$

and the corresponding Reuss lower limits are:

$$K^{\text{Reuss}} = \left(S_{11} + S_{22} + S_{33} + 2\left(S_{12} + S_{13} + S_{23}\right)\right)^{-1} \tag{4.11}$$

$$G^{\text{Reuss}} = 15\left(4\left(S_{11} + S_{22} + S_{33} - S_{12} - S_{13} - S_{23}\right) + 3\left(S_{44} + S_{55} + S_{66}\right)\right)^{-1} \tag{4.12}$$

The values for the Voigt-Reuss-Hill (VRH) bulk and shear moduli are provided in Table 4.7. These values can be compared against K^{VRH} and G^{VRH} for Tobermorite 11 BÅ. We observe that the values are smaller by more than 50% in all three samples and we have a softer material in hybrid cases. Also the values do not show a significant change when the chain length is increased from 6 to 8 which means a plateau is reached for chain lengths above 4. Moreover, the DFT values compare well against FF values. However, this is expected since we already demonstrated good performance of the force field for elastic constants.

Table 4.7: Average elastic parameters (GPa). The upper (Voigt) and lower (Reuss) bounds are computed based on equations 4.9 and 4.11. The average of these two bounds gives the Hill estimates for shear and bulk moduli.

Sample	Method	K^{Voigt}	G^{Voigt}	K^{Reuss}	G^{Reuss}	K^{VRH}	G^{VRH}
tet:C-S-H	DFT	36.28	22.66	30.45	16.25	33.37	19.46
	FF	31.71	19.84	26.98	14.43	29.34	17.13
hex:C-S-H	DFT	27.11	15.62	20.87	7.48	23.99	11.55
	FF	28.62	15.43	22.19	7.37	25.40	11.40
oct:C-S-H	DFT	28.32	15.71	21.50	8.99	24.91	12.35
	FF	25.55	13.36	20.46	7.60	23.01	10.48
Tobermorite 11 Å [132]	DFT	66.7	37.8	55.0	34.1	60.8	36.0

4.7 Applications of the force field to XC-S-H

4.7.1 Thermal conductivity

Now that we have the force field available to us, we can apply the same Green-Kubo theory expounded in section 3.2 to compute thermal conductivity for XC-S-H. Results for tet, hex and oct:C-S-H are presented in table 4.8 and compared with experimental values which are available for hex:C-S-H and oct:C-S-H. We can see that in both cases, simulations

over-estimate the value of thermal conductivity. From the previous sections, we know the overall structures used in simulations are close to what exists in experiments. However, several factors can still contribute to smaller values observed for thermal conductivity in experiments compared to simulations. First, as the elemental analysis in table 4.1 shows, we have impurities such as Na in the system besides what is present in our model which can amplify scattering in the material. Moreover, we are considering only the fully dry case while in reality, we still have some water molecules in the interlayer of the samples which yet again is an additional mechanism for phonon scattering. The next factor is structural order present in the simulated models compared to experimental samples. As X-ray data in figure 4.3 shows, we expect a more disordered in-place structure overall compared to the single cells constructed for simulations. For instance we only considered presence of dimer silicates on the surface of portlandite interlayers while it's possible that we have a mixture of dimers and trimers in experimental samples. Also due to size limitations, turbostratism of the layers has not been taken into account in simulations. Such concerns can be addressed in future research focused on thermal conductivity in XC-S-H Based on findings in Chapter 3, we can also

Table 4.8: Thermal conductivity (W/m.K) computed from Green-Kubo calculations as described in section 3.2. Simulation results are compared to experimental values available for hex:C-S-H and oct:C-S-H

	tet:C-S-H	hex:C-S-H	oct:C-S-H
Exp.	-	0.46 ± 0.034	0.347 ± 0.026
GK	0.751 ± 0.068	0.647 ± 0.079	0.636 ± 0.098
Diffusive (DFT)	0.25	0.16	0.15
Diffusive (FF)	0.28	0.19	0.19

separately calculate the diffusive contribution to thermal conductivity using Allen-Feldman theory[4]. As see in table 4.8, force field results overestimate the diffusive contribution as compared to DFT data. However, they are within 20% of each other which is an acceptable error considering the tolerance we set for elastic parameters when fitting the force field. Moreover, these results provide further evidence that the reduction in thermal conductivity

can be mainly attributed to a change in character of diffusive modes. In other words, if only a comparison is required to assess thermal conductivity between hybrid materials with different chain lengths, it is possible to only rely on diffusive contributions computed based on DFT results. Finally, the force field results can be further improved (if required) by including vibrational information in the fitting data set.

4.7.2 Creep

In this section, we aim to investigate potential applications of XC-S-H for improved creep performance using the developed force field for the hybrid material and the incremental stress marching technique developed in chapter 2. Strain evolution as a function of cycles is plotted in 4.7. These results can be compared to results in Figure 2.11. For C-S-H with H/S=2.9, the basal spacing has a value of about 14 Å. With 5000 cycles, a strain of 7% is reached for those samples. As seen in Figure 4.7, this level of strain corresponds to hex:C-S-H and oct:C-S-H. This regime can be considered a transition from intraglobular to interglobular behavior. We can see that at longer basal spacing were interglobular behavior is becoming dominant, cross-linking can significantly reduce shear strain. For oct:C-S-H we have about 8% compared to 11% for C-S-H at similar basal spacing. The strain figure also paints a different picture of the energy landscape for X:C-S-H compared to C-S-H. As the schematic in Figure 4.7(b) shows, we seem to have major basins (dotted curves) with smaller basins inside which cause the jumps seen in Figure 4.7. This picture is compatible with a fractal picture of the energy landscape[22] and is expected for a complex system such as XC-S-H.

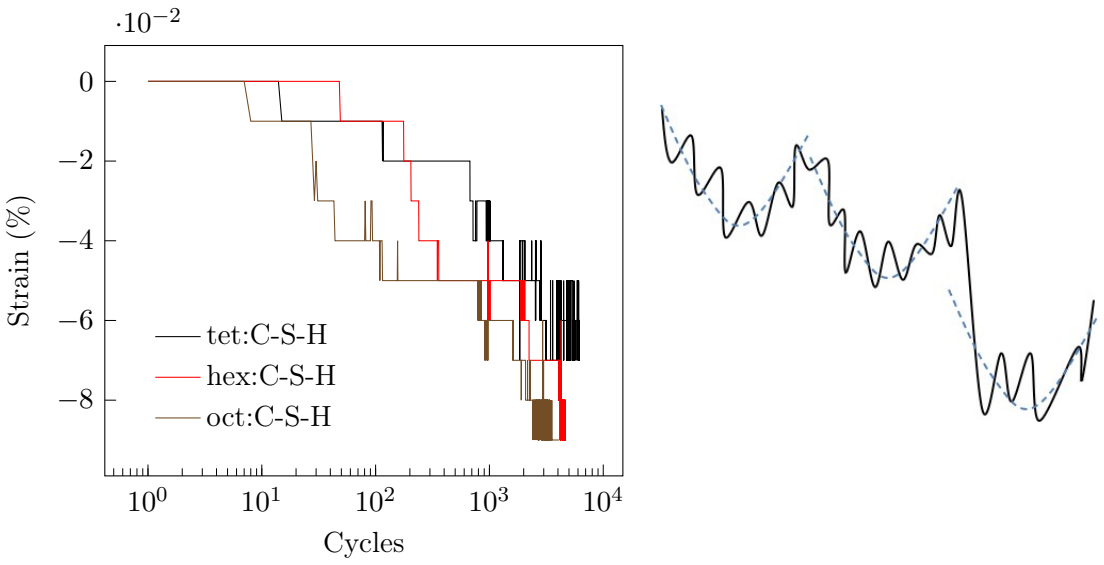

(a) (b)

Figure 4.7: Evolution of strain under constant shear as a function of applied cycles which correspond to temporal evolution (creep).

Chapter 5

Summary and future research

Our purpose in this thesis was to better understand various characteristics of organic and hybrid calcium silicate hydrates which are ubiquitous in construction industry. We adopted a simulation approach which is capable of providing valuable insight at the nanoscale. In the first part of the thesis, we investigate time-dependent mechanical properties (e.g. creep) of C-S-H. The main contributions of this part are as follows:

- A simulation technique (incremental stress marching or ISM) was developed which makes it possible to overcome large energy barriers and study evolution of the material over inaccessibly large time scales.
- At small scales, each C-S-H globule behaves like a viscoelastic material. In other words, there is an asymptote to the time-dependent deformation and unloading causes the material to go back to the initial state. This behavior can be modeled by a stretched exponential function.
- As the water is increased in the interlayer and basal spacing is increased, we transition from a viscoelastic intraglobular behavior to an exponential-logarithmic interglobular

behavior. This demonstrates that logrithmic creep arises from sliding of C-S-H globules over each other rather than logarithmic deformation of the globules themselves.

- Finally, an exponential-logarithmic function is proposed for modeling the combined viscoelastic-creep behavior of C-S-H.

The second part of the thesis explores physics of thermal transport in a prototypical hybrid organic-inorganic material. The contributions of this part are as follows:

- Hybrid organic-inorganic models were constructed by cross-linking interlayer space in Tobermorite 11 Åwith polymers of chain lengths 2, 4, 8 and 10. The INTERFACE force field was adopted for the model which made molecular dynamics simulations possible.
- Using the Green-Kubo theory, thermal conductivity of the material was computed. We found a significant reduction in samples with longer chain lengths.
- To understand the origins of this reduction, a modal analysis was carried out on the models. A method was developed for characterizing propagating modes as opposed to diffusive modes.
- It was found that degrees of freedom corresponding to the polymer molecules, only contribute to localized modes. Moreover, the percentage of propagating modes remains constant. Hence, we can conclude that the reduction in thermal conductivity can be attributed to reduced diffusivities.

In the last part of the thesis, we focused on developing a hybrid material which can be synthesized in the lab and shows great potential for improved performance. The contributions of this section are as follows:

- Using dipodal organosilanes and through a sol-gel process, a hybrid organic-inorganic material was synthesized in the laboratory.

- Through extensive X-ray characterization, we demonstrate that the inorganic layers are cross-linked by organic chains.
- The experimental findings such as basal spacing, density and in-plane X-ray reflections are used to resolve an atomic model for the material.
- An algorithm is developed for curating a quantum mechanically derived force field that is capable of providing accurate material properties such as cell parameters and elastic properties.
- Thermal conductivity and creep properties of the material are explored as demonstrations of what can be done with the developed force field.

It is our hope that these contributions help in moving the cement industry toward a more reliable and sustainable material. There remains so much to be done and the research carried out in this thesis can be further pursued in multiple directions:

- Regarding the techniques developed for simulating time-dependent phenomena, questions remain regarding the exact relationship between shear cycles and time. Synthetic energy landscapes such as the NK model[56] combined with Kinetic Monte Carlo techniques may be able to shed some light on the connection.
- As regards thermal and mechanical properties in hybrid materials, we only investigated cross-linked interlayer spaces. However, single-sided grafting may potentially have lower conductivity as in clay minerals[82] which warrants further investigation through experimental synthesis and simulations.
- At the moment, we are only able to measure creep and elastic properties of XC-S-H though simulations. Experimental techniques need to be developed to be able to measure such nanoscopic properties for XC-S-H.

- In recent years, machine learning force fields have shown potential for accurate modeling of thermal conductivity and other properties in complex systems[67, 65]. Their applicability and accuracy can be explored for hybrid systems.

- For more accurate thermal conductivity modeling, vibrational density of states or density can be included as observables in the fitting process. Although the added computational expense might prove challenging.

- Availability of XCSHFF provides an opportunity to explore other material properties such as fracture toughness even before any experimental measurements are possible.

- In XC-S-H, we ignored the role played by water and assumed completely dry samples. The effect of water content on material behavior merits further investigation. Moreover, impurities may affect the computed conductivities.

Bibliography

[1] Artba (american road & transportation builders administration) bridge report. 2021.

[2] R. Alizadeh, J. J. Beaudoin, and L. Raki. Viscoelastic nature of calcium silicate hydrate. *Cement and Concrete Composites*, 32(5):369–376, 2010.

[3] A. J. Allen, J. J. Thomas, and H. M. Jennings. Composition and density of nanoscale calcium–silicate–hydrate in cement. *Nature materials*, 6(4):311–316, 2007.

[4] P. B. Allen and J. L. Feldman. Thermal conductivity of disordered harmonic solids. *Physical Review B*, 48(17):12581, 1993.

[5] A. Bahadori. *Thermal insulation handbook for the oil, gas, and petrochemical industries*. Gulf Professional Publishing, 2014.

[6] A. Barducci, M. Bonomi, and M. Parrinello. Metadynamics. *Wiley Interdisciplinary Reviews: Computational Molecular Science*, 1(5):826–843, 2011.

[7] M. Bauchy, B. Wang, M. Wang, Y. Yu, M. J. A. Qomi, M. M. Smedskjaer, C. Bichara, F.-J. Ulm, and R. Pellenq. Fracture toughness anomalies: viewpoint of topological constraint theory. *Acta Materialia*, 121:234–239, 2016.

[8] M. Bauchy, M. Wang, Y. Yu, B. Wang, N. A. Krishnan, E. Masoero, F.-J. Ulm, and R. Pellenq. Topological control on the structural relaxation of atomic networks under stress. *Physical review letters*, 119(3):035502, 2017.

[9] Z. Bažant and E. Osman. Double power law for basic creep of concrete. *Matériaux et Construction*, 9(1):3–11, 1976.

[10] Z. P. Bazant and S. Baweja. Creep and shrinkage prediction model for analysis and design of concrete structures: Model b3. *ACI Special Publications*, 194:1–84, 2000.

[11] Z. P. Bazant and S. Prasannan. Solidification theory for concrete creep. i: Formulation. *Journal of engineering mechanics*, 115(8):1691–1703, 1989.

[12] Z. P. Bazant, Q. Yu, G.-H. Li, G. J. Klein, and V. Kristek. Excessive deflections of record-span prestressed box girder. *Concrete International*, 32(6):44–52, 2010.

[13] J. J. Beaudoin, H. Dramé, L. Raki, and R. Alizadeh. Formation and characterization of calcium silicate hydrate–hexadecyltrimethylammonium nanostructure. *Journal of Materials Research*, 23(10):2804–2815, 2008.

[14] R. Bell and P. Dean. Atomic vibrations in vitreous silica. *Discussions of the Faraday society*, 50:55–61, 1970.

[15] P. E. Blöchl. Projector augmented-wave method. *Physical review B*, 50(24):17953, 1994.

[16] J. Blomqvist, L. Ahjopalo, B. Mannfors, and L.-O. Pietilä. Studies on aliphatic polyesters i: Ab initio, density functional and force field studies of esters with one carboxyl group. *Journal of Molecular Structure: THEOCHEM*, 488(1-3):247–262, 1999.

[17] H. J. Böhm and S. Nogales. Mori–tanaka models for the thermal conductivity of composites with interfacial resistance and particle size distributions. *Composites Science and Technology*, 68(5):1181–1187, 2008.

[18] N. Burger, A. Laachachi, M. Ferriol, M. Lutz, V. Toniazzo, and D. Ruch. Review of thermal conductivity in composites: mechanisms, parameters and theory. *Progress in Polymer Science*, 61:1–28, 2016.

[19] A. Cadiau, J. S. Lee, D. Damasceno Borges, P. Fabry, T. Devic, M. T. Wharmby, C. Martineau, D. Foucher, F. Taulelle, C.-H. Jun, et al. Design of hydrophilic metal organic framework water adsorbents for heat reallocation. *Advanced Materials*, 27(32):4775–4780, 2015.

[20] D. G. Cahill and R. Pohl. Heat flow and lattice vibrations in glasses. *Solid State Communications*, 70(10):927–930, 1989.

[21] Y. Chalopin, K. Esfarjani, A. Henry, S. Volz, and G. Chen. Thermal interface conductance in si/ge superlattices by equilibrium molecular dynamics. *Physical Review B*, 85(19):195302, 2012.

[22] P. Charbonneau, J. Kurchan, G. Parisi, P. Urbani, and F. Zamponi. Fractal free energy landscapes in structural glasses. *Nature communications*, 5(1):1–6, 2014.

[23] G. Chen. Size and interface effects on thermal conductivity of superlattices and periodic thin-film structures. *Journal of Heat Transfer*, 1997.

[24] L. Chen, W. Yu, Y. Lu, P. Wu, and F. Han. Characteristics of heat fluxes of an oil pipeline armed with thermosyphons in permafrost regions. *Applied Thermal Engineering*, 190:116694, 2021.

[25] D. R. Clarke and S. R. Phillpot. Thermal barrier coating materials. *Materials today*, 8(6):22–29, 2005.

[26] R. T. Cygan, J.-J. Liang, and A. G. Kalinichev. Molecular models of hydroxide, oxyhydroxide, and clay phases and the development of a general force field. *The Journal of Physical Chemistry B*, 108(4):1255–1266, 2004.

[27] P. Dauber-Osguthorpe, V. A. Roberts, D. J. Osguthorpe, J. Wolff, M. Genest, and A. T. Hagler. Structure and energetics of ligand binding to proteins: Escherichia coli dihydrofolate reductase-trimethoprim, a drug-receptor system. *Proteins: Structure, Function, and Bioinformatics*, 4(1):31–47, 1988.

[28] P. Dauber-Osguthorpe, V. A. Roberts, D. J. Osguthorpe, J. Wolff, M. Genest, and A. T. Hagler. Structure and energetics of ligand binding to proteins: Escherichia coli dihydrofolate reductase-trimethoprim, a drug-receptor system. *Proteins: Structure, Function, and Bioinformatics*, 4(1):31–47, 1988.

[29] F. DeAngelis, M. G. Muraleedharan, J. Moon, H. R. Seyf, A. J. Minnich, A. J. McGaughey, and A. Henry. Thermal transport in disordered materials. *Nanoscale and Microscale Thermophysical Engineering*, 23(2):81–116, 2019.

[30] E. Dechaumphai, D. Lu, J. J. Kan, J. Moon, E. E. Fullerton, Z. Liu, and R. Chen. Ultralow thermal conductivity of multilayers with highly dissimilar debye temperatures. *Nano letters*, 14(5):2448–2455, 2014.

[31] C. Dharmawardhana, M. Bakare, A. Misra, and W.-Y. Ching. Nature of interatomic bonding in controlling the mechanical properties of calcium silicate hydrates. *Journal of the American Ceramic Society*, 99(6):2120–2130, 2016.

[32] E. Durgun, H. Manzano, R. Pellenq, and J. C. Grossman. Understanding and controlling the reactivity of the calcium silicate phases from first principles. *Chemistry of Materials*, 24(7):1262–1267, 2012.

[33] H. Eyring. The activated complex in chemical reactions. *The Journal of Chemical Physics*, 3(2):107–115, 1935.

[34] J. L. Feldman, P. B. Allen, and S. R. Bickham. Numerical study of low-frequency vibrations in amorphous silicon. *Physical Review B*, 59(5):3551, 1999.

[35] R. Feldman and P. Sereda. A new model for hydrated portland cement and its practical implications. *Engineering Journal*, 53(8-9):53–59, 1970.

[36] P. L. Freddolino, F. Liu, M. Gruebele, and K. Schulten. Ten-microsecond molecular dynamics simulation of a fast-folding ww domain. *Biophysical journal*, 94(10):L75–L77, 2008.

[37] F. Fumagalli, S. Bellani, M. Schreier, S. Leonardi, H. C. Rojas, A. Ghadirzadeh, G. Tullii, A. Savoini, G. Marra, L. Meda, et al. Hybrid organic–inorganic h 2-evolving photocathodes: understanding the route towards high performance organic photo-electrochemical water splitting. *Journal of Materials Chemistry A*, 4(6):2178–2187, 2016.

[38] J. D. Gale. Gulp: A computer program for the symmetry-adapted simulation of solids. *Journal of the Chemical Society, Faraday Transactions*, 93(4):629–637, 1997.

[39] S. Galmarini, A. Kunhi Mohamed, and P. Bowen. Atomistic simulations of silicate species interaction with portlandite surfaces. *The Journal of Physical Chemistry C*, 120(39):22407–22413, 2016.

[40] G. Geng, R. J. Myers, M. J. A. Qomi, and P. J. Monteiro. Densification of the interlayer spacing governs the nanomechanical properties of calcium-silicate-hydrate. *Scientific reports*, 7(1):1–8, 2017.

[41] A. Giri, P. E. Hopkins, J. G. Wessel, and J. C. Duda. Kapitza resistance and the thermal conductivity of amorphous superlattices. *Journal of Applied Physics*, 118(16):165303, 2015.

[42] A. Giri, J.-P. Niemelä, C. J. Szwejkowski, M. Karppinen, and P. E. Hopkins. Reduction in thermal conductivity and tunable heat capacity of inorganic/organic hybrid superlattices. *Physical Review B*, 93(2):024201, 2016.

[43] S. Grangeon, F. Claret, Y. Linard, and C. Chiaberge. X-ray diffraction: a powerful tool to probe and understand the structure of nanocrystalline calcium silicate hydrates. *Acta Crystallographica Section B: Structural Science, Crystal Engineering and Materials*, 69(5):465–473, 2013.

[44] S. Grangeon, F. Claret, C. Roosz, T. Sato, S. Gaboreau, and Y. Linard. Structure of nanocrystalline calcium silicate hydrates: insights from x-ray diffraction, synchrotron x-ray absorption and nuclear magnetic resonance. *Journal of applied crystallography*, 49(3):771–783, 2016.

[45] S. Grangeon, B. Lanson, M. Lanson, and A. Manceau. Crystal structure of ni-sorbed synthetic vernadite: a powder x-ray diffraction study. *Mineralogical Magazine*, 72(6):1279–1291, 2008.

[46] S. Grimme. Semiempirical gga-type density functional constructed with a long-range dispersion correction. *Journal of computational chemistry*, 27(15):1787–1799, 2006.

[47] J. Ha, S. Chae, K. Chou, T. Tyliszczak, and P. Monteiro. Effect of polymers on the nanostructure and on the carbonation of calcium silicate hydrates: a scanning transmission x-ray microscopy study. *Journal of materials science*, 47(2):976–989, 2012.

[48] S. Hamid. The crystal structure of the 11å natural tobermorite ca2. 25 [si3o7. 5 (oh) 1.5]· 1h2o. *Zeitschrift für Kristallographie-Crystalline Materials*, 154(3-4):189–198, 1981.

[49] H. Heinz, T.-J. Lin, R. Kishore Mishra, and F. S. Emami. Thermodynamically consistent force fields for the assembly of inorganic, organic, and biological nanostructures: the interface force field. *Langmuir*, 29(6):1754–1765, 2013.

[50] R. Hill. The elastic behaviour of a crystalline aggregate. *Proceedings of the Physical Society. Section A*, 65(5):349, 1952.

[51] E. R. Homer, D. Rodney, and C. A. Schuh. Kinetic monte carlo study of activated states and correlated shear-transformation-zone activity during the deformation of an amorphous metal. *Physical Review B*, 81(6):064204, 2010.

[52] W. G. Hoover. Canonical dynamics: Equilibrium phase-space distributions. *Physical review A*, 31(3):1695, 1985.

[53] M. H. Hubler, R. Wendner, and Z. P. Bažant. Comprehensive database for concrete creep and shrinkage: Analysis and recommendations for testing and recording. *ACI Materials Journal*, 112(4), 2015.

[54] J. W. Hyde and W. J. George. Oil well and method for production of oil through permafrost zone, Oct. 19 1971. US Patent 3,613,792.

[55] K. Ioannidou, K. J. Krakowiak, M. Bauchy, C. G. Hoover, E. Masoero, S. Yip, F.-J. Ulm, P. Levitz, R. J.-M. Pellenq, and E. Del Gado. Mesoscale texture of cement hydrates. *Proceedings of the National Academy of Sciences*, 113(8):2029–2034, 2016.

[56] B. A. Isner and D. J. Lacks. Generic rugged landscapes under strain and the possibility of rejuvenation in glasses. *Physical review letters*, 96(2):025506, 2006.

[57] B. P. Jelle, A. Gustavsen, and R. Baetens. The path to the high performance thermal building insulation materials and solutions of tomorrow. *Journal of Building Physics*, 34(2):99–123, 2010.

[58] H. M. Jennings. Refinements to colloid model of csh in cement: Cm-ii. *Cement and Concrete Research*, 38(3):275–289, 2008.

[59] H. Jónsson, G. Mills, and K. W. Jacobsen. Nudged elastic band method for finding minimum energy paths of transitions. *Classical and Quantum Dynamics in Condensed Phase Simulations*, 1998.

[60] F. B. Juangsa, Y. Muroya, M. Ryu, J. Morikawa, and T. Nozaki. Comparative study of thermal conductivity in crystalline and amorphous nanocomposite. *Applied Physics Letters*, 110(25):253105, 2017.

[61] V. Kanchanason and J. Plank. Role of ph on the structure, composition and morphology of csh–pce nanocomposites and their effect on early strength development of portland cement. *Cement and Concrete Research*, 102:90–98, 2017.

[62] M. Kassner and M. Pérez-Prado. Fundamentals of creep in metals and alloys, elsevier. *Technology & Engineering*, pages 1–279, 2004.

[63] D. Kaya, N. Green, C. Maloney, and M. Islam. Normal modes and density of states of disordered colloidal solids. *Science*, 329(5992):656–658, 2010.

[64] G.-H. Kim, D. Lee, A. Shanker, L. Shao, M. S. Kwon, D. Gidley, J. Kim, and K. P. Pipe. High thermal conductivity in amorphous polymer blends by engineered interchain interactions. *Nature materials*, 14(3):295–300, 2015.

[65] K. Kobayashi, H. Nakamura, A. Yamaguchi, M. Itakura, M. Machida, and M. Okumura. Machine learning potentials for tobermorite minerals. *Computational Materials Science*, 188:110173, 2021.

[66] M. Königsberger, M. Irfan-ul Hassan, B. Pichler, and C. Hellmich. Downscaling based identification of nonaging power-law creep of cement hydrates. *Journal of Engineering Mechanics*, 142(12):04016106, 2016.

[67] P. Korotaev, I. Novoselov, A. Yanilkin, and A. Shapeev. Accessing thermal conductivity of complex compounds by machine learning interatomic potentials. *Physical Review B*, 100(14):144308, 2019.

[68] G. Kovačević, B. Persson, L. Nicoleau, A. Nonat, and V. Veryazov. Atomistic modeling of crystal structure of ca1. 67sihx. *Cement and concrete research*, 67:197–203, 2015.

[69] K. J. Krakowiak, R. G. Nannapaneni, A. Moshiri, T. Phatak, D. Stefaniuk, L. Sadowski, and M. J. A. Qomi. Engineering of high specific strength and low thermal conductivity cementitious composites with hollow glass microspheres for high-temperature high-pressure applications. *Cement and Concrete Composites*, page 103514, 2020.

[70] K. J. Krakowiak, W. Wilson, S. James, S. Musso, and F.-J. Ulm. Inference of the phase-to-mechanical property link via coupled x-ray spectrometry and indentation analysis: Application to cement-based materials. *Cement and Concrete Research*, 67:271–285, 2015.

[71] G. Kresse and J. Hafner. Ab initio molecular dynamics for liquid metals. *Physical Review B*, 47(1):558, 1993.

[72] A. Kumar, B. J. Walder, A. Kunhi Mohamed, A. Hofstetter, B. Srinivasan, A. J. Rossini, K. Scrivener, L. Emsley, and P. Bowen. The atomic-level structure of cementitious calcium silicate hydrate. *The Journal of Physical Chemistry C*, 121(32):17188–17196, 2017.

[73] A. Kushima, J. Eapen, J. Li, S. Yip, and T. Zhu. Time scale bridging in atomistic simulation of slow dynamics: viscous relaxation and defect activation. *The European Physical Journal B*, 82(3):271–293, 2011.

[74] C. Laberty-Robert, K. Valle, F. Pereira, and C. Sanchez. Design and properties of functional hybrid organic–inorganic membranes for fuel cells. *Chemical Society Reviews*, 40(2):961–1005, 2011.

[75] D. J. Lacks and M. J. Osborne. Energy landscape picture of overaging and rejuvenation in a sheared glass. *Physical review letters*, 93(25):255501, 2004.

[76] J. M. Larkin and A. J. McGaughey. Thermal conductivity accumulation in amorphous silica and amorphous silicon. *Physical Review B*, 89(14):144303, 2014.

[77] M. Lee and B. Barr. An overview of the fatigue behaviour of plain and fibre reinforced concrete. *Cement and Concrete Composites*, 26(4):299–305, 2004.

[78] D. Lenzen, P. Bendix, H. Reinsch, D. Fröhlich, H. Kummer, M. Möllers, P. P. Hügenell, R. Gläser, S. Henninger, and N. Stock. Scalable green synthesis and full-scale test of the metal–organic framework cau-10-h for use in adsorption-driven chillers. *Advanced Materials*, 30(6):1705869, 2018.

[79] X. Li, Z. Grasley, E. J. Garboczi, and J. W. Bullard. Modeling the apparent and intrinsic viscoelastic relaxation of hydrating cement paste. *Cement and Concrete Composites*, 55:322–330, 2015.

[80] J. Liu, B. Yoon, E. Kuhlmann, M. Tian, J. Zhu, S. M. George, Y.-C. Lee, and R. Yang. Ultralow thermal conductivity of atomic/molecular layer-deposited hybrid organic–inorganic zincone thin films. *Nano letters*, 13(11):5594–5599, 2013.

[81] S.-Q. Liu, D.-Y. Tan, K.-Q. Zhang, X.-L. Ji, Y. Tao, and Y.-X. Fu. *Protein folding, binding and energy landscape: A synthesis*. INTECH Open Access Publisher Retrieved from, 2012.

[82] M. D. Losego, I. P. Blitz, R. A. Vaia, D. G. Cahill, and P. V. Braun. Ultralow thermal conductivity in organoclay nanolaminates synthesized via simple self-assembly. *Nano letters*, 13(5):2215–2219, 2013.

[83] M. D. Losego, M. E. Grady, N. R. Sottos, D. G. Cahill, and P. V. Braun. Effects of chemical bonding on heat transport across interfaces. *Nature materials*, 11(6):502–506, 2012.

[84] D. L. Malandro and D. J. Lacks. Relationships of shear-induced changes in the potential energy landscape to the mechanical properties of ductile glasses. *The Journal of chemical physics*, 110(9):4593–4601, 1999.

[85] T. A. Manz and N. G. Limas. Introducing ddec6 atomic population analysis: part 1. charge partitioning theory and methodology. *RSC advances*, 6(53):47771–47801, 2016.

[86] H. Manzano, E. Masoero, I. Lopez-Arbeloa, and H. M. Jennings. Shear deformations in calcium silicate hydrates. *Soft Matter*, 9(30):7333–7341, 2013.

[87] S. Masoumi, D. Ebrahimi, H. Valipour, and M. J. Abdolhosseini Qomi. Nanolayered attributes of calcium-silicate-hydrate gels. *Journal of the American Ceramic Society*, 103(1):541–557, 2020.

[88] S. Masoumi, H. Valipour, and M. J. Abdolhosseini Qomi. Intermolecular forces between nanolayers of crystalline calcium-silicate-hydrates in aqueous medium. *The Journal of Physical Chemistry C*, 121(10):5565–5572, 2017.

[89] S. Masoumi, S. Zare, H. Valipour, and M. J. Abdolhosseini Qomi. Effective interactions between calcium-silicate-hydrate nanolayers. *The Journal of Physical Chemistry C*, 123(8):4755–4766, 2019.

[90] H. Matsuyama and J. Young. Effects of ph on precipitation of quasi-crystalline calcium silicate hydrate in aqueous solution. *Advances in cement research*, 12(1):29–33, 2000.

[91] H. Matsuyama and J. F. Young. Intercalation of polymers in calcium silicate hydrate: a new synthetic approach to biocomposites? *Chemistry of materials*, 11(1):16–19, 1999.

[92] H. Matsuyama and J. F. Young. Synthesis of calcium silicate hydrate/polymer complexes: Part i. anionic and nonionic polymers. *Journal of Materials Research*, 14(8):3379–3388, 1999.

[93] F. Merlin, H. Lombois, S. Joly, N. Lequeux, J.-L. Halary, and H. Van Damme. Cement-polymer and clay-polymer nano-and meso-composites: spotting the difference. *Journal of Materials Chemistry*, 12(11):3308–3315, 2002.

[94] S. Merlino, E. Bonaccorsi, and T. Armbruster. Tobermorites: Their real structure and order-disorder (od) character. *American Mineralogist*, 84(10):1613–1621, 1999.

[95] J. Minet, S. Abramson, B. Bresson, C. Sanchez, V. Montouillout, and N. Lequeux. New layered calcium organosilicate hybrids with covalently linked organic functionalities. *Chemistry of materials*, 16(20):3955–3962, 2004.

[96] A. Minnich, M. S. Dresselhaus, Z. Ren, and G. Chen. Bulk nanostructured thermoelectric materials: current research and future prospects. *Energy & Environmental Science*, 2(5):466–479, 2009.

[97] S. H. Mir, L. A. Nagahara, T. Thundat, P. Mokarian-Tabari, H. Furukawa, and A. Khosla. Organic-inorganic hybrid functional materials: An integrated platform for applied technologies. *Journal of The Electrochemical Society*, 165(8):B3137–B3156, 2018.

[98] R. A. Miron and K. A. Fichthorn. Multiple-time scale accelerated molecular dynamics: Addressing the small-barrier problem. *Physical review letters*, 93(12):128301, 2004.

[99] R. K. Mishra, A. K. Mohamed, D. Geissbühler, H. Manzano, T. Jamil, R. Shahsavari, A. G. Kalinichev, S. Galmarini, L. Tao, H. Heinz, et al. cemff: A force field database for cementitious materials including validations, applications and opportunities. *Cement and Concrete Research*, 102:68–89, 2017.

[100] R. K. Mishra, A. K. Mohamed, D. Geissbühler, H. Manzano, T. Jamil, R. Shahsavari, A. G. Kalinichev, S. Galmarini, L. Tao, H. Heinz, et al. cemff: A force field database for cementitious materials including validations, applications and opportunities. *Cement and Concrete Research*, 102:68–89, 2017.

[101] H. Mizuno, S. Mossa, and J.-L. Barrat. Beating the amorphous limit in thermal conductivity by superlattices design. *Scientific reports*, 5:14116, 2015.

[102] H. Mohammadhosseini, R. Alyousef, N. H. A. S. Lim, M. M. Tahir, H. Alabduljabbar, and A. M. Mohamed. Creep and drying shrinkage performance of concrete composite comprising waste polypropylene carpet fibres and palm oil fuel ash. *Journal of Building Engineering*, 30:101250, 2020.

[103] P. J. Monteiro, G. Geng, D. Marchon, J. Li, P. Alapati, K. E. Kurtis, and M. J. A. Qomi. Advances in characterizing and understanding the microstructure of cementitious materials. *Cement and Concrete Research*, 124:105806, 2019.

[104] J. Moon, B. Latour, and A. J. Minnich. Propagating elastic vibrations dominate thermal conduction in amorphous silicon. *Physical Review B*, 97(2):024201, 2018.

[105] A. Morshedifard, S. Masoumi, and M. A. Qomi. Nanoscale origins of creep in calcium silicate hydrates. *Nature communications*, 9(1):1–10, 2018.

[106] A. Moshiri, D. Stefaniuk, S. K. Smith, A. Morshedifard, D. F. Rodrigues, M. J. A. Qomi, and K. J. Krakowiak. Structure and morphology of calcium-silicate-hydrates cross-linked with dipodal organosilanes. *Cement and Concrete Research*, 133:106076, 2020.

[107] G. Munaò, A. Pizzirusso, A. Kalogirou, A. De Nicola, T. Kawakatsu, F. Müller-Plathe, and G. Milano. Molecular structure and multi-body potential of mean force in silica-polystyrene nanocomposites. *Nanoscale*, 10(46):21656–21670, 2018.

[108] R. G. Palmer, D. L. Stein, E. Abrahams, and P. W. Anderson. Models of hierarchically constrained dynamics for glassy relaxation. *Physical Review Letters*, 53(10):958, 1984.

[109] M. Parrinello and A. Rahman. Crystal structure and pair potentials: A molecular-dynamics study. *Physical review letters*, 45(14):1196, 1980.

[110] M. Parrinello and A. Rahman. Polymorphic transitions in single crystals: A new molecular dynamics method. *Journal of Applied physics*, 52(12):7182–7190, 1981.

[111] R. J.-M. Pellenq, A. Kushima, R. Shahsavari, K. J. Van Vliet, M. J. Buehler, S. Yip, and F.-J. Ulm. A realistic molecular model of cement hydrates. *Proceedings of the National Academy of Sciences*, 106(38):16102–16107, 2009.

[112] B. Peters. *Reaction rate theory and rare events*. Elsevier, 2017.

[113] J. Phillips. Stretched exponential relaxation in molecular and electronic glasses. *Reports on Progress in Physics*, 59(9):1133, 1996.

[114] S. Plimpton. Fast parallel algorithms for short-range molecular dynamics. Technical report, Sandia National Labs., Albuquerque, NM (United States), 1993.

[115] S. Plimpton. Fast parallel algorithms for short-range molecular dynamics. *Journal of computational physics*, 117(1):1–19, 1995.

[116] E. Pustovgar, R. P. Sangodkar, A. S. Andreev, M. Palacios, B. F. Chmelka, R. J. Flatt, and J.-B. d. de Lacaillerie. Understanding silicate hydration from quantitative analyses of hydrating tricalcium silicates. *Nature communications*, 7(1):1–9, 2016.

[117] X. Qian, X. Gu, and R. Yang. Anisotropic thermal transport in organic–inorganic hybrid crystal β-znte (en) 0.5. *The Journal of Physical Chemistry C*, 119(51):28300–28308, 2015.

[118] X. Qian, X. Gu, and R. Yang. Thermal conductivity modeling of hybrid organic-inorganic crystals and superlattices. *Nano Energy*, 41:394–407, 2017.

[119] M. A. Qomi, K. Krakowiak, M. Bauchy, K. Stewart, R. Shahsavari, D. Jagannathan, D. B. Brommer, A. Baronnet, M. J. Buehler, S. Yip, et al. Combinatorial molecular optimization of cement hydrates. *Nature communications*, 5(1):1–10, 2014.

[120] M. J. A. Qomi, M. Bauchy, F.-J. Ulm, and R. J.-M. Pellenq. Anomalous composition-dependent dynamics of nanoconfined water in the interlayer of disordered calcium-silicates. *The Journal of chemical physics*, 140(5):054515, 2014.

[121] M. J. A. Qomi, F.-J. Ulm, and R. J.-M. Pellenq. Physical origins of thermal properties of cement paste. *Physical Review Applied*, 3(6):064010, 2015.

[122] S. Rahimi-Aghdam, Z. P. Bažant, and M. A. Qomi. Cement hydration from hours to centuries controlled by diffusion through barrier shells of csh. *Journal of the Mechanics and Physics of Solids*, 99:211–224, 2017.

[123] A. Reuß. Berechnung der fließgrenze von mischkristallen auf grund der plastizitätsbedingung für einkristalle. *ZAMM-Journal of Applied Mathematics and Mechanics/Zeitschrift für Angewandte Mathematik und Mechanik*, 9(1):49–58, 1929.

[124] P. Richard, M. Nicodemi, R. Delannay, P. Ribiere, and D. Bideau. Slow relaxation and compaction of granular systems. *Nature materials*, 4(2):121–128, 2005.

[125] I. G. Richardson. The calcium silicate hydrates. *Cement and concrete research*, 38(2):137–158, 2008.

[126] I. G. Richardson. Model structures for c-(a)-sh (i). *Acta Crystallographica Section B: Structural Science, Crystal Engineering and Materials*, 70(6):903–923, 2014.

[127] S. Rogge, L. Vanduyfhuys, A. Ghysels, M. Waroquier, T. Verstraelen, G. Maurin, and V. Van Speybroeck. A comparison of barostats for the mechanical characterization of metal–organic frameworks. *Journal of chemical theory and computation*, 11(12):5583–5597, 2015.

[128] P. Saikia, A. Borah, R. L. Goswamee, et al. Hybrid nanocomposites of layered double hydroxides: an update of their biological applications and future prospects. *Colloid and Polymer Science*, 295(5):725–747, 2017.

[129] C. Sanchez, B. Julián, P. Belleville, and M. Popall. Applications of hybrid organic–inorganic nanocomposites. *Journal of Materials Chemistry*, 15(35-36):3559–3592, 2005.

[130] H. R. Seyf and A. Henry. A method for distinguishing between propagons, diffusions, and locons. *Journal of Applied Physics*, 120(2):025101, 2016.

[131] M. Shahidi, B. Pichler, and C. Hellmich. Viscous interfaces as source for material creep: a continuum micromechanics approach. *European Journal of Mechanics-A/Solids*, 45:41–58, 2014.

[132] R. Shahsavari, R. J.-M. Pellenq, and F.-J. Ulm. Empirical force fields for complex hydrated calcio-silicate layered materials. *Physical Chemistry Chemical Physics*, 13(3):1002–1011, 2011.

[133] F. Shalchy and N. Rahbar. Nanostructural characteristics and interfacial properties of polymer fibers in cement matrix. *ACS applied materials & interfaces*, 7(31):17278–17286, 2015.

[134] S. Shen, A. Henry, J. Tong, R. Zheng, and G. Chen. Polyethylene nanofibres with very high thermal conductivities. *Nature nanotechnology*, 5(4):251, 2010.

[135] J.-P. Shih, S.-Y. Sheu, and C.-Y. Mou. A voronoi polyhedra analysis of structures of liquid water. *The Journal of chemical physics*, 100(3):2202–2212, 1994.

[136] J. Shim, D.-G. Kim, J. H. Lee, J. H. Baik, and J.-C. Lee. Synthesis and properties of organic/inorganic hybrid branched-graft copolymers and their application to solid-state electrolytes for high-temperature lithium-ion batteries. *Polymer Chemistry*, 5(10):3432–3442, 2014.

[137] L. Skinner, S. Chae, C. Benmore, H. Wenk, and P. Monteiro. Nanostructure of calcium silicate hydrates in cements. *Physical review letters*, 104(19):195502, 2010.

[138] A. G. Skirtach, D. G. Kurth, and H. Möhwald. Laser-embossing nanoparticles into a polymeric film. *Applied Physics Letters*, 94(9):093106, 2009.

[139] A. G. Skirtach, M. S. Saveleva, K. Eftekhari, A. Abalymov, T. E. Douglas, D. Volodkin, and B. V. Parakhonskiy. Hierarchy of hybrid materials–the place of inorganics-in-organics in it, their composition and applications. *Frontiers in chemistry*, 7:179, 2019.

[140] S. Soyer-Uzun, S. R. Chae, C. J. Benmore, H.-R. Wenk, and P. J. Monteiro. Compositional evolution of calcium silicate hydrate (c–s–h) structures by total x-ray scattering. *Journal of the American Ceramic Society*, 95(2):793–798, 2012.

[141] S. Spirk, G. Findenig, A. Doliska, V. E. Reichel, N. L. Swanson, R. Kargl, V. Ribitsch, and K. Stana-Kleinschek. Chitosan–silane sol–gel hybrid thin films with controllable layer thickness and morphology. *Carbohydrate polymers*, 93(1):285–290, 2013.

[142] Z. Tang, N. A. Kotov, S. Magonov, and B. Ozturk. Nanostructured artificial nacre. *Nature materials*, 2(6):413–418, 2003.

[143] H. Taylor. Nanostructure of c-s-h: Current status. *Advanced cement based materials*, 1(1):38–46, 1993.

[144] H. F. Taylor. Bound water in cement pastes and its significance for pore solution compositions. *MRS Online Proceedings Library (OPL)*, 85, 1986.

[145] W. J. Thrift, C. Q. Nguyen, M. Darvishzadeh-Varcheie, S. Zare, N. Sharac, R. N. Sanderson, T. J. Dupper, A. I. Hochbaum, F. Capolino, M. J. Abdolhosseini Qomi, et al. Driving chemical reactions in plasmonic nanogaps with electrohydrodynamic flow. *ACS nano*, 11(11):11317–11329, 2017.

[146] A. Tlili, V. Giordano, Y. Beltukov, P. Desmarchelier, S. Merabia, and A. Tanguy. Enhancement and anticipation of the ioffe–regel crossover in amorphous/nanocrystalline composites. *Nanoscale*, 11(44):21502–21512, 2019.

[147] L. Ukrainczyk, R. Bellman, and A. Anderson. Template synthesis and characterization of layered al- and mg- silsesquioxanes. *The Journal of Physical Chemistry B*, 101(4):531–539, 1997.

[148] F.-J. Ulm, M. Vandamme, C. Bobko, J. Alberto Ortega, K. Tai, and C. Ortiz. Statistical indentation techniques for hydrated nanocomposites: concrete, bone, and shale. *Journal of the American Ceramic Society*, 90(9):2677–2692, 2007.

[149] M. Vandamme and F.-J. Ulm. Nanogranular origin of concrete creep. *Proceedings of the National Academy of Sciences*, 106(26):10552–10557, 2009.

[150] M. Vandamme and F.-J. Ulm. Nanoindentation investigation of creep properties of calcium silicate hydrates. *Cement and Concrete Research*, 52:38–52, 2013.

[151] W. Voight. Lehrbuch der kristallphysik. *Teubner, Leipzig*, 1928.

[152] A. F. Voter. Hyperdynamics: Accelerated molecular dynamics of infrequent events. *Physical Review Letters*, 78(20):3908, 1997.

[153] X. Wei and T. Luo. Chain length effect on thermal transport in amorphous polymers and a structure–thermal conductivity relation. *Physical Chemistry Chemical Physics*, 21(28):15523–15530, 2019.

[154] B. T. Wong and P. M. Mengüç. *Thermal transport for applications in micro/nanomachining*. Springer Science & Business Media, 2008.

[155] E. Worrell, L. Price, N. Martin, C. Hendriks, and L. O. Meida. Carbon dioxide emissions from the global cement industry. *Annual review of energy and the environment*, 26(1):303–329, 2001.

[156] J. Wu and Q. Jia. The heterogeneous energy landscape expression of kww relaxation. *Scientific reports*, 6(1):1–10, 2016.

[157] S.-L. Wu, F. Liu, H.-C. Yang, and S. B. Darling. Recent progress in molecular engineering to tailor organic–inorganic interfaces in composite membranes. *Molecular Systems Design & Engineering*, 2020.

[158] D. J. Wuebbles, D. W. Fahey, K. A. Hibbard, J. R. Arnold, B. DeAngelo, S. Doherty, D. R. Easterling, J. Edmonds, T. Edmonds, T. Hall, et al. Climate science special report: Fourth national climate assessment (nca4), volume i. 2017.

[159] P. Yu and R. Kirkpatrick. Thermal dehydration of tobermorite and jennite. *Concrete Science and Engineering*, 1(3):185–191, 1999.

[160] Y. Yu, M. Wang, D. Zhang, B. Wang, G. Sant, and M. Bauchy. Stretched exponential relaxation of glasses at low temperature. *Physical review letters*, 115(16):165901, 2015.

[161] J. Zhang, G. Qu, and H. Jin. Estimates on thermal effects of the china–russia crude oil pipeline in permafrost regions. *Cold regions science and technology*, 64(3):243–247, 2010.

[162] Q. Zhao, J. Yu, G. Geng, J. Jiang, and X. Liu. Effect of fiber types on creep behavior of concrete. *Construction and Building Materials*, 105:416–422, 2016.

[163] Y. Zhou, A. Morshedifard, J. Lee, and M. J. Abdolhosseini Qomi. The contribution of propagons and diffusons in heat transport through calcium-silicate-hydrates. *Applied Physics Letters*, 110(4):043104, 2017.

[164] T. Zhu and E. Ertekin. Phonons, localization, and thermal conductivity of diamond nanothreads and amorphous graphene. *Nano letters*, 16(8):4763–4772, 2016.

[165] T. Zhu, J. Li, and S. Yip. Atomistic reaction pathway sampling: the nudged elastic band method and nanomechanics applications. *Nano and Cell Mechanics: Fundamentals and Frontiers*, pages 311–338, 2013.